Monthly Notices of the ROYAL ASTRONOMICAL SOCIETY

MNRAS **533,** 2948–2965 (2024)
Advance Access publication 2024 August 14

https://doi.org/10.1093/mnras/stae1970

A big red dot: scattered light, host galaxy signatures, and multiphase gas flows in a luminous, heavily reddened quasar at cosmic noon

Matthew Stepney,[1★†] Manda Banerji,[1] Shenli Tang,[1] Paul C. Hewett,[2] Matthew J. Temple,[3] Clare F. Wethers,[4] Annagrazia Puglisi[1] and Stephen J. Molyneux[1]

[1]*School of Physics and Astronomy, University of Southampton, Southampton SO17 1BJ, UK*
[2]*Institute of Astronomy, University of Cambridge, Madingley Road, Cambridge CB3 0HA, UK*
[3]*Department of Physics, Centre for Extragalactic Astronomy, Durham University, South Road, Durham DH1 3LE, UK*
[4]*Department of Space, Earth and Environment, Chalmers University of Technology, Onsala Space Observatory, SE-439 92 Onsala, Sweden*

Accepted 2024 August 12. Received 2024 August 7; in original form 2024 July 4

ABSTRACT

We present a deep X-Shooter rest-frame ultraviolet (UV) to optical spectral analysis of the heavily reddened quasar, ULASJ2315+0143 at $z = 2.566$, known to reside in a major-merger host galaxy. The rest-frame optical is best fit by a dust-reddened quasar ($E(B-V)^{\rm QSO} = 1.55$) with black-hole mass $\log_{10}(\mathrm{H}\beta, \mathrm{MBH}[\mathrm{M}_\odot]) = 10.26 \pm 0.05$, bolometric luminosity $\mathrm{L_{Bol}} = 10^{48.16}\,\mathrm{erg\,s^{-1}}$ and Eddington-scaled accretion rate $\log_{10}(\lambda_{\rm Edd}) = -0.19$. We find remarkable similarities between ULASJ2315+0143 and the high-redshift little red dots (LRDs). The rest-frame UV cannot be explained by a dusty quasar component alone and requires an additional blue component consistent with either a star-forming host galaxy or scattered AGN light. We detect broad high-ionization emission lines in the rest-UV, supporting the scattered light interpretation for the UV excess. The scattering fraction represents just 0.05 per cent of the total luminosity of ULASJ2315+0143. Analysis of the mid-infrared SED suggests an absence of hot dust on torus-scales similar to what is observed for LRDs. The obscuring medium is therefore likely on galaxy scales. We detect narrow, blueshifted associated absorption-line systems in C IV, N V, Si IV, and Si III. There is evidence for significant high-velocity ($>1000\,\mathrm{km\,s^{-1}}$) outflows in both the broad- and narrow-line regions as traced by C IV and [O III] emission. The kinetic power of the [O III] wind is $\dot{\epsilon}_k^{ion} = 10^{44.61}\mathrm{erg\,s^{-1}} \sim 0.001\,\mathrm{L_{Bol}}$. ULASJ2315+0143 is likely in an important transition phase where star formation, black-hole accretion and multiphase gas flows are simultaneously occurring.

Key words: galaxy: evolution – galaxies: active – quasars: individual..

1 INTRODUCTION

Key to understanding the evolution of massive galaxies is the study of feedback driven by active galactic nuclei (AGN) powered by the central supermassive black holes in galaxies. Cosmological simulations have demonstrated that feedback processes are pivotal to explaining a multitude of observables, such as the $M-\sigma$ relation (Magorrian et al. 1998; Kormendy & Ho 2013; Habouzit et al. 2021), the shape of the galaxy luminosity and stellar mass function (Cole et al. 2001; Benson et al. 2003; Huang et al. 2003; Somerville et al. 2008; Schaye et al. 2015) and the observed morphologies and colours of present-day galaxies (Dubois et al. 2016; Pillepich et al. 2017).

It is likely that most massive galaxies have undergone at least one major merger event to account for the mass distribution of massive galaxies in the local Universe (Conselice et al. 2003; López-Sanjuan et al. 2012). In such a paradigm of massive galaxy formation, rapid gas inflow to the nucleus fuels a powerful quasi-stellar object (QSO) whilst simultaneously inducing a starburst phase (Di Matteo, Springel & Hernquist 2005; Hopkins et al. 2005, 2008). The starburst galaxies are shrouded in dust, appearing as either ultraluminous infrared galaxies or sub-mm galaxies (Veilleux et al. 2009; Simpson et al. 2014). The same gas supply that fuels star formation also fuels accretion on to the central supermassive black hole, which is initially dust obscured (Granato et al. 2004; Di Matteo et al. 2005; Hopkins & Elvis 2009). Powerful feedback processes can then couple energy and momentum from the accreting supermassive black hole (SMBH) to the interstellar medium (ISM) quenching star formation during a 'blow-out' phase (Fabian 2012; Harrison & Ramos Almeida 2024) with the presence of dust potentially making radiatively driven outflows during this phase more efficient (e.g. Ishibashi, Banerji & Fabian 2017; Costa et al. 2018).

Red quasars, which show dust extinction affecting the quasar UV continuum have been postulated to correspond to this 'blow-out' phase in massive galaxy formation (Urrutia, Lacy & Becker 2008; Banerji et al. 2012; Glikman et al. 2012, 2015; Assef et al. 2015; Banerji et al. 2015; Calistro Rivera et al. 2021). A variety of different methods have been used to select red quasars with varying levels of extinction including optical (e.g. Klindt et al. 2019; Fawcett et al. 2020), near-infrared (NIR; e.g. Glikman et al. 2012; Banerji et al. 2015) and mid-infrared (e.g. Eisenhardt et al. 2012;

★ E-mail: ms10g17@soton.ac.uk
† Anniversary Fellow.

© 2024 The Author(s).
Published by Oxford University Press on behalf of Royal Astronomical Society. This is an Open Access article distributed under the terms of the Creative Commons Attribution License (https://creativecommons.org/licenses/by/4.0/), which permits unrestricted reuse, distribution, and reproduction in any medium, provided the original work is properly cited.

Downloaded from https://academic.oup.com/mnras/article/533/3/2948/7733827 by guest on 07 November 2024

Assef et al. 2015) colour selections. Many red quasars are found to reside in major mergers (e.g. Urrutia et al. 2008; Glikman et al. 2015; Banerji et al. 2021). Powerful feedback signatures have also been detected in several of these populations, although it is debated whether these feedback processes are more efficient in the obscured quasar phase relative to the unobscured quasar phase. For example, extreme broad-line region (BLR) and narrow-line region (NLR) outflows have been reported among populations of extremely red quasars (ERQs; Hamann et al. 2017; Perrotta et al. 2019; Gillette et al. 2024), with their kinetic power exceeding that of blue quasars at comparable luminosities (Zakamska et al. 2016; Perrotta et al. 2019). The correlation between dust extinction and radio emission in mildly obscured red quasars in Sloan Digital Sky Survey (SDSS) has been interpreted as evidence for low-power radio jets or winds causing shocks in a dusty environment (Fawcett et al. 2023). On the other hand, some studies have found very similar ionized gas outflow properties between red and blue quasars when the two samples are matched in luminosity and redshift (e.g. Temple et al. 2019; Fawcett et al. 2022). Spatially resolved observations of multiphase outflows in red quasars are also now starting to uncover the complex gas dynamics in these systems (e.g. Wylezalek et al. 2022; Veilleux et al. 2023).

Ground-based surveys of the most luminous obscured quasars at $z \sim 1-4$ suggest they could dominate the number densities at the highest intrinsic luminosities implying that this population of previously unstudied AGN may account for some of the most luminous and massive accreting black holes at cosmic noon (Assef et al. 2015; Banerji et al. 2015). More recently an abundant population of little red dots (LRDs) observed with *JWST* has emerged, many of which are postulated to be obscured AGN, hundreds of times more common than UV-bright AGN at the faint end of the luminosity function (Kocevski et al. 2023; Onoue et al. 2023; Greene et al. 2024; Kocevski et al. 2024). Therefore, the obscured phase of supermassive black hole growth also appears to be increasingly important at lower luminosities, and in the high-redshift Universe.

Intriguingly, despite their red colour selection, several of the red quasar populations appear to show excess emission at rest-frame UV wavelengths that is inconsistent with an AGN SED affected by dust extinction (e.g. Assef et al. 2015, 2020, 2022; Wethers et al. 2018; Noboriguchi et al. 2019; Kocevski et al. 2023, 2024; Greene et al. 2024; Matthee et al. 2024; Pérez-González et al. 2024; Williams et al. 2024). In the population of Hot Dust Obscured Galaxies (HotDOGs), polarization studies attribute the UV excess to a scattered light component from the heavily cocooned AGN (Assef et al. 2020). In ERQs, the extreme column densities ($N_{\rm H} \gtrsim 10^{24}\,{\rm cm}^{-1}$) reported are suggestive of a dense circumnuclear gas cloud suppressing the accretion disc emission (Goulding et al. 2018). Spectropolarimetry studies of this population also suggest scattering from equatorial dusty disc-winds as the primary cause of their UV emission (Alexandroff et al. 2018). Furthermore, ~ 20 per cent of the broad-line AGN recently observed with *JWST* are both obscured and feature relatively blue colours in the rest-frame UV, with many more unconfirmed AGN candidates demonstrating similar photometry (Kocevski et al. 2023, 2024; Greene et al. 2024; Matthee et al. 2024). The broad-band UV excess can be explained by a scattered light component or emission from unobscured star-forming regions in the AGN host galaxy (Greene et al. 2024) and spectroscopic observations would help to discriminate between these scenarios.

In this paper, we conduct a detailed study of a heavily reddened quasar (HRQs), ULASJ2315+0143 at $z \sim 2.56$. HRQs are one class of red quasars selected based on their red NIR colours. Over 60 HRQs have been selected using NIR and mid-infrared colour selections using data from the United Kingdom Infrared Deep Sky Survey (UKIDSS), VISTA, and WISE surveys (Banerji et al. 2012, 2013, 2015; Temple et al. 2019). They cover a redshift range $0.7 \lesssim z \lesssim 2.7$ and have measured dust extinctions of $0.5 \lesssim E(B-V) \lesssim 3.0$. In the X-ray, HRQs are amongst the most powerful quasars known, with a median $\langle {\rm L}_{2-10\,{\rm kev}} \rangle = 10^{45.1}\,{\rm erg\,s}^{-1}$ (Lansbury et al. 2020). As expected from the heavy attenuation observed in the rest-frame optical, HRQs have large gas column densities $N_{\rm H} \sim 10^{22}-10^{23}\,{\rm cm}^{-2}$, suggestive of a blow-out phase given their high Eddington-scaled accretion rates (Lansbury et al. 2020). Atacama Large Millimeter/submillimeter Array (ALMA) observations have revealed diverse gas fractions, gas morphologies and ISM properties in HRQs (Banerji et al. 2017, 2018, 2021). Finally, deep broad-band optical photometry of a sub-sample of 17 HRQs reveals that at least 10 feature blue colours in the rest-frame UV inconsistent with the dust-reddened quasar SED in the rest-frame optical. The UV-excess potentially originates from relatively unobscured star-forming host galaxies with average ${\rm SFR_{UV}} = 130 \pm 95\,{\rm M_\odot\,yr^{-1}}$ (Wethers et al. 2018). However, spectroscopic data in the rest-frame UV are required to confirm this hypothesis.

We selected ULASJ2315+0143 for follow-up with X-Shooter due to its detection at rest-frame UV wavelengths across multiple bands in the HyperSuprimeCam (HSC) survey as well as the rich array of multiwavelength observations already assembled for this source. X-ray data suggest that the inner regions of ULASJ2315+0143 are dominated by a powerful accreting SMBH ($L_X = 3 \times 10^{45}\,{\rm erg\,s}^{-1}$) with moderately high gas column densities ($N_{\rm H} \sim 10^{22}\,{\rm cm}^{-2}$), making it the ideal candidate for studying radiation-driven winds (Lansbury et al. 2020). At longer wavelengths, ULASJ2315+0143 has been confirmed to be undergoing a gas-rich major merger via ALMA observations of the warm molecular gas as traced by CO(3-2) (Banerji et al. 2021). Further CO(1-0) observations from the very large array (VLA) confirm that the merging galaxies reside within an extended reservoir of cold molecular gas, spatially offset from the merging pair and redshifted with respect to the CO(3-2) observations (Banerji et al. 2018). In addition, ALMA observations of the dust continuum suggest a total star formation rate of $\sim 680\,{\rm M_\odot\,yr^{-1}}$, consistent with a merger-induced starburst. In the rest-frame optical, ULASJ2315+0143 is amongst the reddest of the HRQ sample and hence exhibits the most unambiguous evidence of excess rest-frame UV emission (Wethers et al. 2018). Owing to its broad wavelength coverage, the analysis of the X-Shooter spectrum will enable the detailed study of ULASJ2315+0143 across the entire rest-frame UV to optical wavelength region, leading to a better understanding of the UV excess emission and probing key diagnostic emission and absorption features that enable the study of multiphase and multiscale winds.

The paper is organized as follows: Section 2 details the observations and reduction of the X-Shooter spectrum. In Section 3, we model the spectral energy distribution and analyse the emission and absorption line properties. We discuss our results in Section 4 in the context of other red AGN populations. Our conclusions are presented in Section 5. Vacuum wavelengths and AB magnitudes are employed throughout the paper and we adopt a Lambda cold dark matter cosmology with $h_0 = 0.71$, $\Omega_{\rm M} = 0.27$, and $\Omega_\Lambda = 0.73$.

2 SPECTRAL OBSERVATIONS & DATA REDUCTION

We observed ULASJ2315+0143 (RA = 348.9842, Dec. = 1.7307) with the X-Shooter spectrograph on the very large telescope (VLT) (see Data Availability for access to the raw data). X-Shooter is an

Downloaded from https://academic.oup.com/mnras/article/533/3/2948/7733827 by guest on 07 November 2024

Echelle spectrograph installed on the UT2 telescope at the VLT (Vernet et al. 2011). It is comprised of three arms; the Ultra-Violet/Blue (UVB), the Visible (VIS), and the NIR. The combined wavelength coverage of X-Shooter ranges from ∼3100–24000 Å, enabling the study of both the rest-frame UV and rest-frame optical emission of ULASJ2315+0143 at $z \sim 2.5$. The spectra were obtained using a 2×2 binning to minimize read-out noise. Slit widths were set to 1.3 arcsec for the UVB and 1.2 arcsec for both the VIS and NIR arms, yielding a spectral resolution $R = 4100$, 6500, 4300, for the UVB, VIS, and NIR arms, respectively. The target was observed for ∼9 h based on its broad-band SED (Wethers et al. 2018) and to ensure sufficient signal-to-noise ratio (S/N) across the entire wavelength range covered by X-Shooter. To aid scheduling, these observations were split into roughly 1 h long observing blocks and a standard ABBA nodding pattern was adopted for the purposes of sky subtraction in the NIR arm.

We employ PYPEIT v1.14.0,[1] a PYTHON package for semi-automated reduction of astronomical slit-based spectroscopy (Prochaska et al. 2020a; 2020b), for the spectral reduction. Some user-level parameters had to be adjusted from their default values and these are detailed in Appendix A. Wavelength calibrations in the X-Shooter UVB/VIS arms were conducted by matching arc lines from Thorium–Argon (ThAr) lamps to the inbuilt ThAr arc line catalogue stored within PYPEIT. For the NIR arm, wavelength calibrations were conducted using the OH sky line transitions from the spectrum itself. PYPEITs extraction algorithm is based on Horne (1986). A third-order polynomial fit is attempted across all orders in a given exposure. Echelle objects are retained if the S/N of the trace exceeds a certain threshold value in all orders, or if the S/N of the trace exceeds the minimum S/N threshold over a user-defined number of orders (see Appendix A for details). The standard star trace is used as a crutch for the polynomial fit for those orders that do not exceed the minimum S/N requirement. The relative flux calibration was conducted within PYPEIT, and the spectrum was then normalized to the cModel magnitude of the quasar from Hyper Suprime-Cam (HSC) in the g, i, and z bands,[2] and the UKIDSS magnitudes in the H and K bands (Banerji et al. 2015).

Fig. 1 depicts the full flux-calibrated 1D X-Shooter spectrum of ULASJ2315+0143 , as well as the corresponding noise spectrum. As expected from the red NIR colour of ULASJ2315+143 ($(H - K) > 1.4$; Banerji et al. 2015), the NIR spectral shape (middle/bottom panel; Fig. 1) is consistent with significant dust attenuation toward the quasar continuum. The median continuum S/N in the intervals [16000, 17000] Å and [21 000, 22 000] Å are ∼ 13 and ∼ 12 Å^{-1}, respectively. We observe narrow emission lines, including [O II] λλ3726, 3729 and [O III] λλ4960, 5008 in the NIR spectrum. However, there is no discernible signal from either [Ne III] λ3869 or [Ne V] λ3426. We see several broad Balmer lines in the NIR, including the Hγ λ4342, Hβ λ4863, and Hα λ6565 emission. The median continuum S/N in the interval [6000, 10 000] Å is ∼ 1 Å^{-1} (top/right; Fig. 1). When rebinned by a factor of 10, the median continuum S/N ∼ 0.2Å^{-1}, hence the flux in this region is dominated by noise. The median continuum S/N in the interval [4600, 4900] Å (top/left panel; Fig. 1) is ∼ 15 Å^{-1}. The rest-frame UV emission is inconsistent with the attenuation observed at redder wavelengths, which would predict a much lower UV flux. We see broad Lyα, N V, and C IV emission features on a blue UV continuum. We also observe a strong narrow component to the Lyα emission as well as absorption around the Lyα and C IV emission-line profiles. These spectral features are fully explored in Section 3.3.

[1]https://github.com/pypeit/PypeIt/tree/1.14.0

[2]Calibration to the Dark Energy Camera photometry for this source yields $\Delta g = 0.06$ mag (Wethers et al. 2018), hence we estimate an ∼ 6 per cent uncertainty in the flux calibration

3 RESULTS

3.1 Rest-frame UV image decomposition

We begin by conducting image decomposition analysis to better understand the source of the rest-frame UV emission in ULASJ2315+0143 . We consider the morphology of this emission as traced by the imaging data from HSC in the g band. We follow the work of Silverman et al. (2020) and Tang et al. (2021) to perform a 2D image decomposition analysis on the HSC g-band image of ULASJ2315+0143 , which covers 4000–5500 Å in the observed frame (Kawanomoto et al. 2018). We apply the tool GALIGHT (Galaxy shapes of Light, Ding et al. 2022), which was developed based on the image modelling capabilities of LENSTRONOMY (Birrer et al. 2021). The tool accepts a preset of number of point sources to be used in fitting. We tested three cases: (i) no point source (i.e. no AGN contribution to the rest-frame UV), (ii) one point source (i.e. a single quasar contribution to the rest-frame UV), and (iii) two-point sources (i.e. a dual quasar contribution to the rest-frame UV). As a result, the algorithm failed to find a secondary point source in the third case, and favoured at most one point source in the region. The algorithm then finds as many extended sources as necessary in the field, and fits them with Sérsic profiles simultaneously with the point sources. We show the results in Fig. 2, with the first row showing the case of no point source and the second row showing the model for one point source. For the model with one point source, we also show the image after subtracting the point source model from the data (second row, second column). The third column shows the normalized residual of the fitting. The final column shows the 1D annulus light profiles from the centre of the source to the outer regions. The reconstructed models are shown by the blue curves, in comparison with the data, shown by the open circles. The bottom sub-panels show the fractional residuals in 1D.

We find that the light profile of this system can either be explained by one point spread function (PSF) and four Sérsic profiles or just four Sérsic profiles. We also compared the reduced χ^2 of the two fits, which are 1.09 for the model without a point source, and 1.04 for the model with a point source. We therefore conclude that the rest-frame UV morphology of this source can be equally well reconstructed with and without a PSF contribution to the g band. We are therefore motivated to explore spectral energy distribution (SED) models that exploit both star-forming host galaxy emission or blue quasar emission.

3.2 Spectral energy distribution

In this section, we explore the rest-frame UV to optical SED of ULASJ2315+0143 . As noted from Fig. 1, the spectral shape is inconsistent with a single reddened quasar SED with excess blue flux detected in the UVB arm relative to this SED. Motivated by Fig. 2, we explore two distinct possibilities to explain the excess UVB flux – (i) a blue quasar component either originating from leaked/scattered light or a secondary AGN and (ii) a star-forming host galaxy. We model the quasar components using the QSOGEN[3]

[3]https://github.com/MJTemple/qsogen

Downloaded from https://academic.oup.com/mnras/article/533/3/2948/7733827 by guest on 07 November 2024

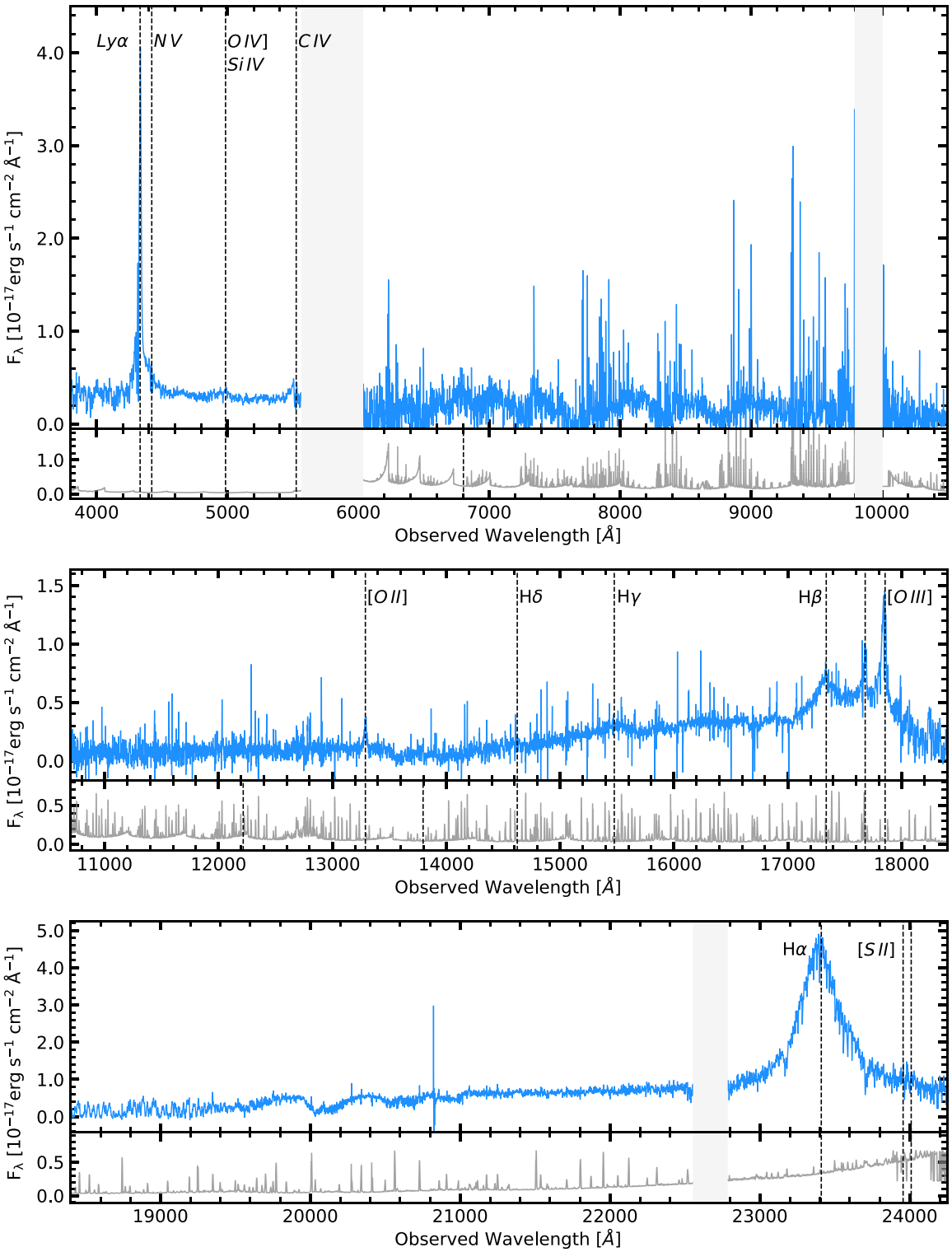

Figure 1. The full flux calibrated 1D spectrum of ULASJ2315+0143 is presented in the top panels of each exert (blue). In addition, the corresponding noise spectrum is presented in the lower panels (grey). Noise spikes marking the transition between arms at ∼ 5800 and ∼ 10 000 Å have been masked out, as too has a region of high noise redward of the Hα emission. Prominent emission lines are marked by dashed vertical black lines and labelled accordingly.

Downloaded from https://academic.oup.com/mnras/article/533/3/2948/7733827 by guest on 07 November 2024

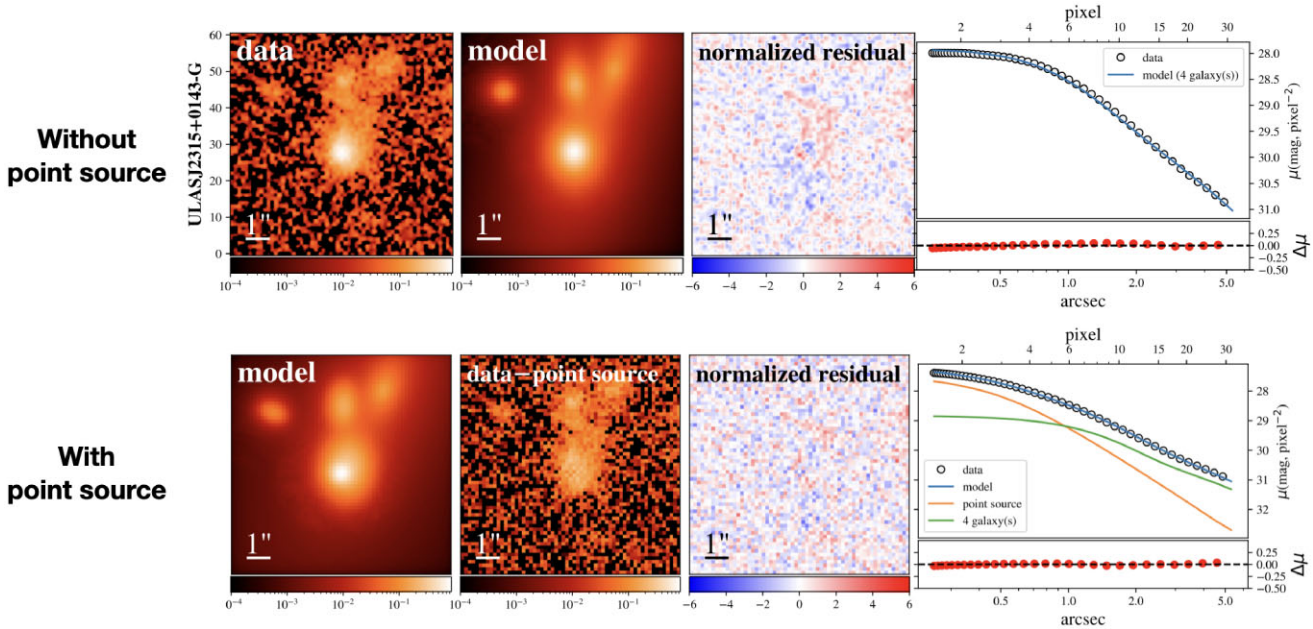

Figure 2. GALIGHT-fitting results on the HSC g-band image of ULASJ2315+0143 . The first row shows the case when use a model incorporating only the Sérsic profiles. The second row shows the case when we include one point source in the model. The reconstructed images are shown by the second and first panel of the rows, respectively. In the second panel of second row, we also show the image after subtracting the point source model from the data. The third column shows the 2D normalized residual map of the fitting. The final column shows the 1D annulus light profiles for the data and the reconstructed model, with the fractional residual shown in the bottom sub-panel.

tool, a PYTHON package that implements an empirically motivated parametric model to simulate quasar colours, magnitudes and SEDs (Temple, Hewett & Banerji 2021b). The host galaxy component is modelled using the BAGPIPES[4] package. Model fits were conducted using a Bayesian Markov chain Monte Carlo (MCMC) method. We utilize EMCEE, a PYTHON package[5] that explores the likelihood space using the affine-invariant ensemble sampler proposed by Goodman & Weare (2010).

3.2.1 *Reddened quasar + blue quasar light*

The first model explored is the combination of a reddened quasar SED with some blue AGN component representing a fraction of the total quasar luminosity leaked/scattered along our line of sight or a less luminous secondary AGN. The free parameters are the luminosity of the primary quasar, $\log_{10}\{\lambda L_\lambda(3000\mathring{A})[\mathrm{erg\ s^{-1}}]\}$, the dust reddening of the primary quasar, $E(B-V)^{\mathrm{QSO}}$ and the fraction of the total intrinsic SED of the primary quasar emitted in the rest-frame UV, f_{UV}. QSOGEN also allows flexibility in the emission-line contributions to the quasar SED via the *emline_type* parameter, which essentially controls the equivalent widths (EWs) of the key quasar emission lines (Temple et al. 2021b). Hence, we also set the *emline_type* as a free parameter in the fit. The model includes no contribution from the quasar host galaxy to the SED. The quasar extinction law assumed by QSOGEN is discussed in section 2.6 of Temple et al. (2021b) and is similar to those derived by Czerny et al. (2004) and Gallerani et al. (2010). We permit the EMCEE package to explore an N-dimensional Gaussian likelihood function, where N represents the number of free parameters in the fit ($N = 4$), and apply uniform priors. Regions significantly affected by telluric absorption are excluded from the SED fit. The best-fitting SED is presented in Fig. 3 overlaid on the X-Shooter spectrum.

The model is able to successfully reproduce the spectrum redward of ∼4200 Å as well as the broad shape of the SED blueward of 1600 Å. However, in the interval [2900, 3800] Å , the continuum is overestimated. The best-fitting parameters of this model are presented in Table 1 (see Appendix B for a discussion on model parameter degeneracies), the quoted uncertainties represent the Monte Carlo uncertainties on the free parameters and hence do not account for the uncertainties associated with the flux calibration. The reddening of the quasar is estimated to be $E(B-V)^{\mathrm{QSO}} = 1.552 \pm 0.002$, which is consistent with the results from SED fitting to the broad-band photometry conducted by Wethers et al. (2018). The dust-corrected optical luminosity is estimated to be $\log_{10}\{\lambda L_\lambda(3000\mathring{A})[\mathrm{erg\ s^{-1}}]\} = 47.907 \pm 0.003$. Only 0.0450 ± 0.0003 per cent of this intrinsic quasar luminosity is required to be scattered or leaked into our line of sight to reproduce the UVB flux. This is a much smaller fraction than is reported in other obscured AGN populations at similar redshifts (e.g. ∼1–3 per cent in HotDOGs; Assef et al. 2020). We will discuss these results further in Section 4.1.

The primary weakness of this SED model is that it is unable to reproduce the narrow [O II] emission as well as overpredicting the continuum flux in the interval [2900, 3800] Å. Strong [O II] emission in the absence of [Ne III] and [Ne V] could be attributed to ongoing star formation (Maddox 2018). Despite the need for an AGN component to explain the broad UV emission lines, it is unclear to what extent the AGN is contributing to the continuum.

3.2.2 *Reddened quasar + star-forming host galaxy*

The second model explored is then the combination of a star-forming host galaxy and dust-reddened quasar SED. We model the

[4]https://github.com/ACCarnall/bagpipes
[5]https://github.com/dfm/emcee

Downloaded from https://academic.oup.com/mnras/article/533/3/2948/7733827 by guest on 07 November 2024

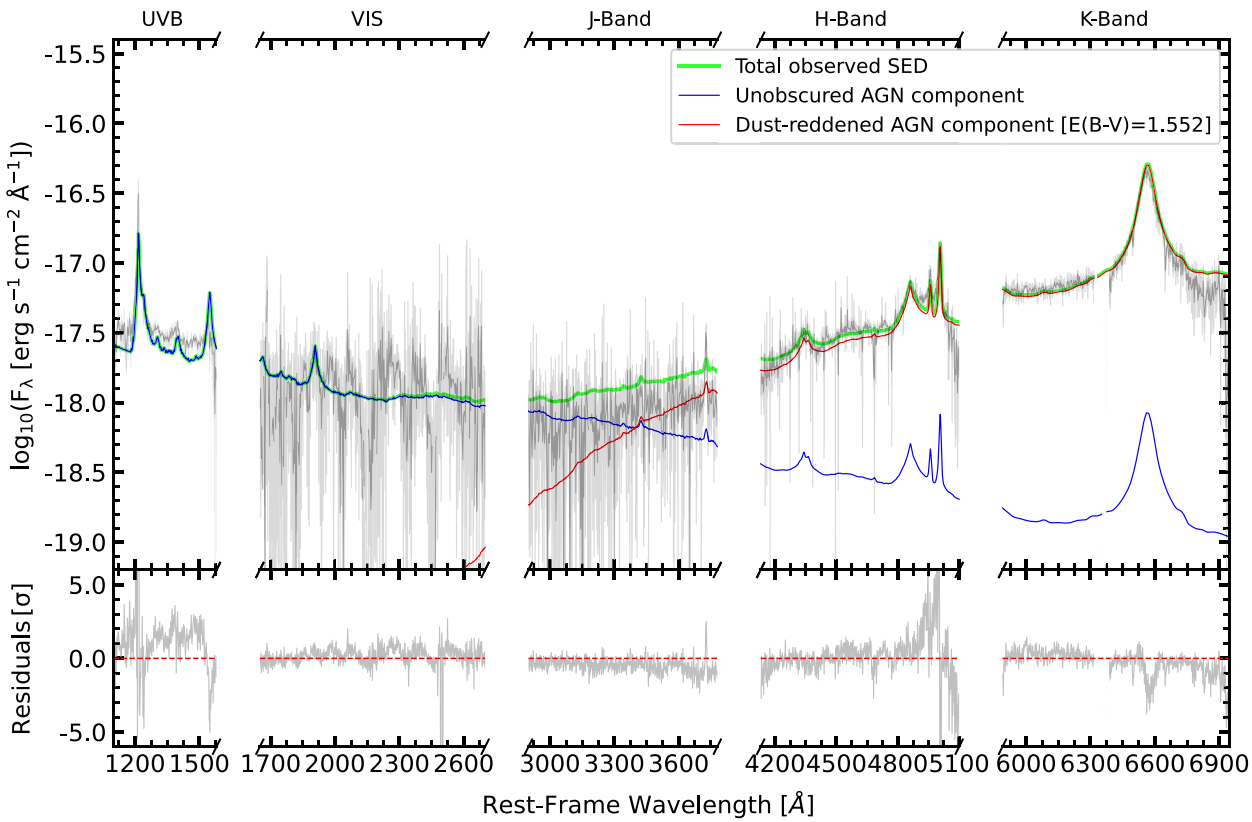

Figure 3. We present the spectrum of ULASJ2315+0143 in light grey with the 20-pixel rebinned spectrum overlaid in dark grey. Our best-fitting SED model is plotted in green. The unobscured AGN component is presented in blue, while the dust-reddened AGN component is presented in red. Regions of high telluric absorption have been masked to aid readership. The bottom panel illustrates the model residuals.

Table 1. Best-fitting QSOGEN parameters for the SED fit shown in Fig. 3.

Parameter	Best-fitting value
emline_type	1.71 ± 0.01
$E(B-V)^{\rm QSO}$ (mag)	1.552 ± 0.002
$\log_{10}\{\lambda L_\lambda(3000\AA)[\rm erg\ s^{-1}]\}$	47.907 ± 0.003
$f_{\rm UV}$	0.0450 ± 0.0003 per cent

Notes. Uncertainties represent the MCMC uncertainties.

host galaxy spectrum using BAGPIPES. We assume a burst-like star formation history (SFH), consistent with the observation of a gas-rich major merger in the ULASJ2315+0143 system (Banerji et al. 2021). Our goal is to find whether a reasonable star-forming galaxy SED model can reproduce the observed UV-continuum shape. Given the dominance of the quasar emission in the rest-frame optical, we do not necessarily expect to obtain robust constraints on the host galaxy properties.

We set the duration of the burst, the stellar mass of the galaxy, $\log(M_*/M_\odot)$, the galaxy dust extinction $A_V^{\rm Gal}$, the metallicity, $\log_{10}(Z/Z_\odot)$ and ionization parameter, $\log_{10}(U)$ as free parameters in the MCMC simulation. We set flat priors on the metallicity and ionization parameter in the range $-2 < \log_{10}(Z/Z_\odot) < 0.3$ and $-3.5 < \log_{10}(U) < -1$. We assume the Calzetti et al. (2000) extinction law. Finally, we set Gaussian priors on the optical luminosity of the quasar, quasar emission line type and quasar dust extinction, defining the position and width of the priors by the best-fitting values and uncertainties of these parameters from Table 1.

The results are presented in Fig. 4. We are able to better reproduce the narrow [O II] emission and broad continuum shape in the interval [2900, 3800] Å with the inclusion of a star-forming galaxy to the SED model. While the star-forming galaxy component is unable to reproduce the broad emission lines observed blueward of 1600 Å, the broad continuum shape at these bluer wavelengths is also well fit by the star-forming galaxy. The best-fitting parameters for this SED model are presented in Table 2, again the uncertainties presented represent the Monte Carlo errors only, and do not account for uncertainties in the flux calibration.

First, we note that the quasar dust attenuation and continuum luminosity for this model are consistent with the values predicted by the previous SED model, confirming that the continuum at redder wavelengths is indeed quasar dominated. We do not place particular emphasis on the physical values of the galaxy parameters in the fit given the degeneracies between these parameters. The lack of data straddling the 4000 Å break, which falls within the gap between the J and H bands, prevents us from placing strong constraints on the stellar mass of the host galaxy and the value of the stellar mass from the SED fit should therefore not be interpreted as representing the total stellar mass of the quasar host. The best-fitting ionization parameter of $-\log_{10}(U) = 1.001 \pm 0.007$ is high for a star-forming galaxy (Costa et al. 2018), but can almost certainly be explained by some AGN contamination to the emission lines, many of which have broad components. Nevertheless, we can conclude that a star-forming galaxy SED can reproduce the UV continuum shape and narrow emission-line features seen in the X-Shooter spectrum.

Downloaded from https://academic.oup.com/mnras/article/533/3/2948/7733827 by guest on 07 November 2024

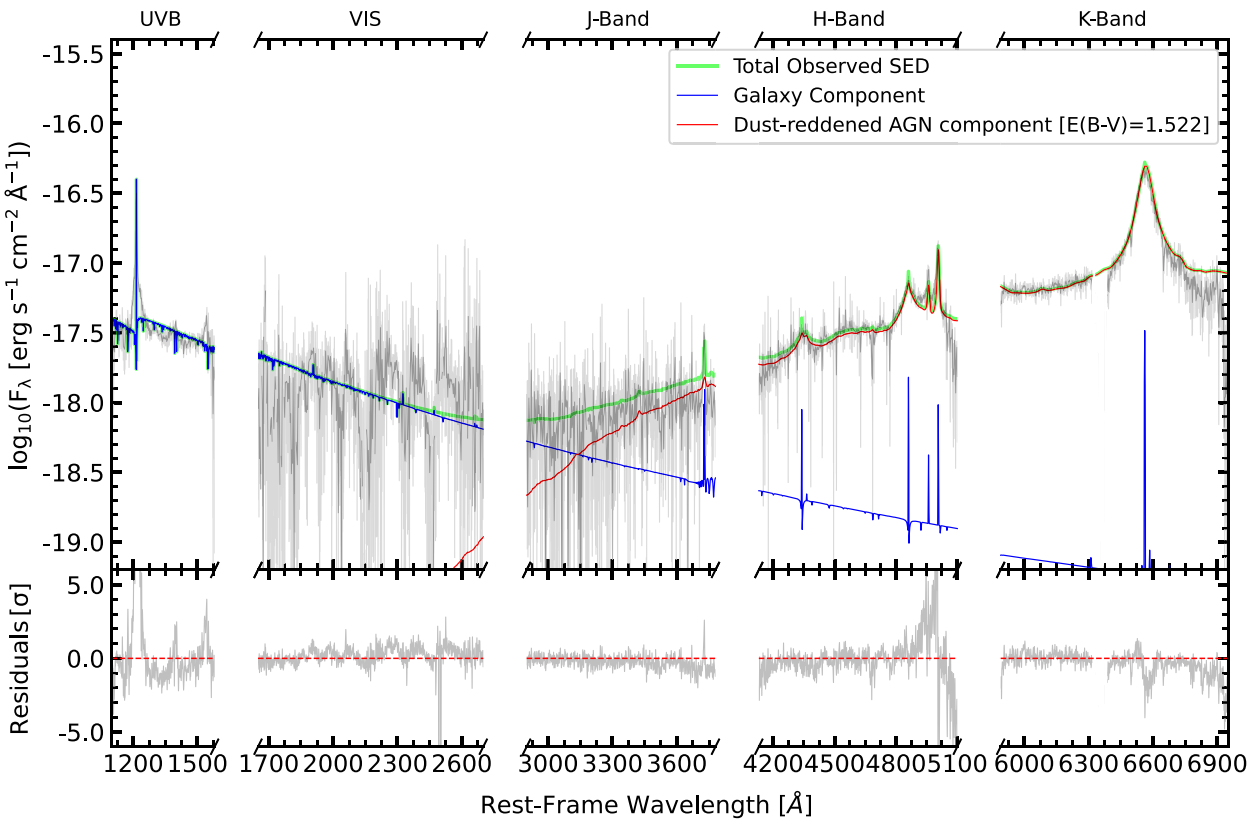

Figure 4. Same as Fig. 3, but instead the rest-frame UV is modelled by a star-forming galaxy, generated using BAGPIPES.

Table 2. QSOGEN and BAGPIPES user-level parameters for the SED fit shown in Fig. 4.

Parameter	Best-fitting value
emline_type	1.24 ± 0.02
$E(B-V)^{\rm QSO}$ (mag)	1.522 ± 0.003
$\log_{10}\{\lambda L_\lambda(3000\AA)[\rm erg\ s^{-1}]\}$	47.901 ± 0.004
$A_{\rm V}^{\rm Gal}$ (mag)	0.41 ± 0.03
$\log_{10}(M_*/{\rm M}_\odot)$	9.47 ± 0.02
$t_{\rm Burst}$ (Myr)	10.4 ± 0.7
$\log_{10}({\rm U})$	$> -1.001 \pm 0.007$
$\log_{10}({\rm Z/Z}_\odot)$	1.70 ± 0.04

Notes. Uncertainties represent the MCMC uncertainties.

If we assume that the entire rest-frame UV continuum originates from young stellar populations, we can calculate a maximum SFR for ULASJ2315+0143 using the following equation:

$$\mathrm{SFR_{FUV}(M_\odot\,yr^{-1}) = \log_{10}(\lambda L_\lambda(1550\,\AA)) + \log_{10}(C_{FUV})}, \quad (1)$$

where the continuum flux at 1550Å, $\lambda L_\lambda(1550\,\AA) = 10^{44.8}\mathrm{erg\,s^{-1}}$ and $\log_{10}(\mathrm{C_{FUV}}) = 43.35$ (Hao et al. 2011; Murphy et al. 2011; Kennicutt & Evans 2012). Equation (1) yields $\mathrm{SFR_{FUV}} = 88\,\mathrm{M_\odot\,yr^{-1}}$, consistent with the SFR estimated for this object using broad-band photometry ($130 \pm 95\,\mathrm{M_\odot\,yr^{-1}}$; Wethers et al. 2018).

3.2.3 *Reddened quasar + blue quasar light + star-forming host galaxy*

Figs 3 and 4 show that both an AGN SED and a star-forming galaxy SED can reproduce the broad continuum shape of the UVB spectrum. With both strong narrow [O II] in the *J* band and broad C IV and N V in the UVB arm a model that combines a star-forming host galaxy with a blue quasar component to reproduce the flux seems well motivated. This is also justified by the image decomposition in Fig. 2, which suggests that both point-like and extended emission contribute to the rest-frame UV flux of this source.

However, the parameters dictating the nebular emission line strength, such as metallicity, ionization parameter and age, are degenerate with the stellar mass. A less massive star-forming galaxy with strong nebular emission makes a similar contribution to the total SED as a more massive galaxy with weaker nebular emission. Furthermore, the stellar mass of the galaxy is degenerate with the fraction of the primary quasar contribution to the UV flux, f_{UV}. Consequently, with all three components of the SED, the fit failed to converge tending to the limits set by the priors on the stellar mass, metallicity, and ionization parameter. We therefore did not explore a three-component SED model further but conclude that the observed spectrum and UV image analysis suggests contributions from both a star-forming host galaxy and a blue AGN component in the UV.

3.3 Emission- and absorption-line properties

We now turn our attention to analysing the spectral-line properties. We utilize the PYQSOFIT package,[6] a python code developed by Guo, Shen & Wang (2018) for all line fits. In all cases uncertainties on line properties are derived by sampling 500 spectra perturbed by

[6]https://github.com/legolason/PyQSOFit

Downloaded from https://academic.oup.com/mnras/article/533/3/2948/7733827 by guest on 07 November 2024

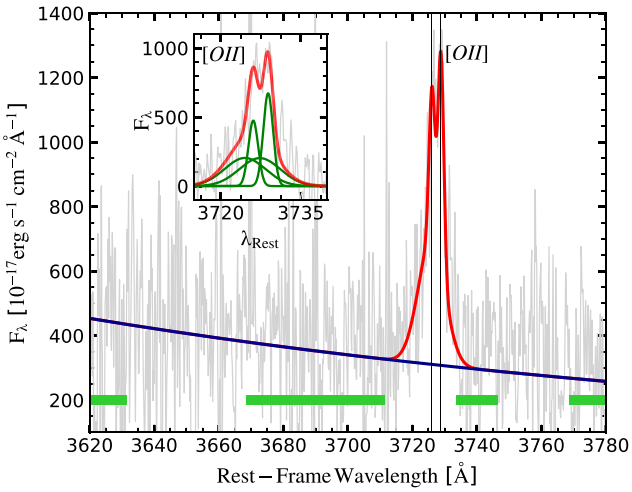

Figure 5. *J*-band spectrum for ULASJ2315+0143 with a dust correction, $E(B-V)^{QSO} = 1.55$, applied in grey and showing the [O II] doublet. The continuum is presented in navy blue, and the windows over which the continuum was fitted are denoted by the thick, lime-green lines. The final fit of the spectrum is presented in red. The smaller panel shows the continuum subtracted total fit in red. The broad components contributing to the total fit are presented in blue and the narrow components are presented in green.

Gaussian noise consistent with the noise array and looking at the mean properties and scatter on these properties from the simulated spectra.

3.3.1 Systemic redshift and star formation rate from [O II]

We begin with an analysis of the NIR arm, which traces the rest-frame optical emission in this object. We fit the *J*-, *H*-, and *K*-band spectra separately so that the continuum fitting is not affected by telluric absorption.

The *J* band contains the narrow [O II] line. The [O II] doublet is spectrally resolved and provides a good indicator of the systemic redshift. The previous best systemic redshift estimate of ULASJ2315+0143 was calculated using the CO(3−2) emission line from ALMA data, yielding $z_{sys} = 2.566$ (Banerji et al. 2021). We fit the [O II] emission doublet without the PYQSOFIT iron template, since the wavelength coverage is too restricted to constrain the fit. A set of broad and a set of narrow components, whose widths and velocity offsets are tied, are used to represent the quasar and galaxy emission. We present the results in Fig. 5. We estimate a redshift, $z_{sys} = 2.5656 \pm 0.0005$ from [O II] which is entirely consistent with the value derived from the CO(3-2) line and is adopted as the systemic redshift for the remainder of the paper.

We can also estimate a value for the instantaneous, unobscured SFR of any host galaxy component using [O II] emission line luminosity by assuming that the line flux does not have any contributions from the AGN. We note, however, that even under this assumption, the [O II] line flux can be significantly affected by both dust extinction and metallicity. Since it is unclear to what degree the line is affected by dust extinction relative to the quasar continuum, we estimate lower limits on the [O II] line luminosity and SFR([O II]), assuming $E(B-V) = 0$ towards the star-forming regions in the host galaxy. We calculate the SFR([O II]) with the following equation:

$$\mathrm{SFR}_{[\mathrm{O\,II}]}(\mathrm{M}_\odot\ \mathrm{yr}^{-1}) = (1.4 \pm 0.4) \times 10^{-41}\mathrm{L}([\mathrm{O\,II}]), \quad (2)$$

where the [O II] line luminosity $\mathrm{L}([\mathrm{O\,II}]) = 10^{42.34} \pm 10^{0.10}$erg s^{-1} for ULASJ2315+0143 (Kennicutt 1998). Equation (2) then yields an $\mathrm{SFR}_{[\mathrm{O\,II}]} = 31.1 \pm 9.3\mathrm{M}_\odot\ \mathrm{yr}^{-1}$.

3.3.2 Black-hole mass, Eddington ratio, and narrow-line region outflows

From Section 3.2, it is clear that redward of 4200 Å the spectrum is dominated by the dust-reddened Type 1 QSO component. For this reason, we apply a dust correction, using the $E(B-V)^{QSO} = 1.55$ estimate from Table 1 to both the *H* and *K* bands before fitting the spectral lines. We model the Hγ emission with a single broad component. The Hβ emission was modelled by two broad components and an additional narrow component. Both [O III] lines were modelled by a single broad component paired with an additional narrow line contribution whose widths and velocity offsets were tied. In the *K* band, we model Hα with two broad components and a single narrow component. Additionally, we model the [S II]$\lambda\lambda$6716, 6730 emission doublet with a further two narrow components, whose widths and velocity offsets are tied. Due to the extreme Hα emission strength, we are unable to robustly model the narrow [N II] emission. The results are presented in Figs 6 and 7.

Using these fits, we estimate the EW, full width half-maximum (FWHM), emission line blueshifts and S/N for each emission line. We define emission line blueshifts using the following equation:

$$V_{50} = \mathrm{c}(\lambda_\mathrm{r} - \lambda_{50})/\lambda_\mathrm{r}\ \ [\mathrm{km\ s^{-1}}], \quad (3)$$

where c is the velocity of light, λ_{50} is the rest-frame wavelength that bisects the 50th percentile line flux and λ_r is the rest-frame wavelength of a given emission feature. The use of line centroids to define blueshifts reflects the well-known line asymmetries of some emission features such as C IV (Richards et al. 2011; Rankine et al. 2020; Stepney et al. 2023; Temple et al. 2023). Furthermore, for the [O III] emission, we also calculate the W80=V90−V10, since the [O III] emission line width is often used as an indicator of NLR outflows (e.g. Shen 2016; Coatman et al. 2019; Perrotta et al. 2019; Temple et al. 2019; Villar Martín et al. 2020). V10 and V90 are calculated using equation (3), evaluated at the 10th and 90th percentile of the line flux, respectively. The S/N of the emission lines are estimated by calculating the ratio between the maximum continuum-subtracted flux and the mean noise across the emission line feature. A summary of the quasar emission line properties can be found in Table 3.

We observe broad blue wings associated with the [O III] emission in Fig. 6, which is reflected in the large line width, W80 = 1830±350 km s^{-1}. The estimated [O III] line luminosity, L([O III]) = $10^{43.71} \pm 10^{0.04}$erg s^{-1}. Our estimate of L([O III]) is sensitive to dust extinction, hence this value serves as a lower limit assuming $E(B-V) = 0$ since we do not know to what extent the NLR is affected by the attenuation suffered by the quasar continuum. The presence of significant line blueshifts in the [O III] emission is consistent with the high UV/optical continuum luminosity estimated by the SED fitting in Section 3.2 and the large L([O III]). The [O II] emission centroid is located at the systemic redshift by definition.

The Balmer lines are very broad as seen in Table 3. We calculate the SMBH mass, M_{BH}, of ULASJ2315+0143 from the measured width

Downloaded from https://academic.oup.com/mnras/article/533/3/2948/7733827 by guest on 07 November 2024

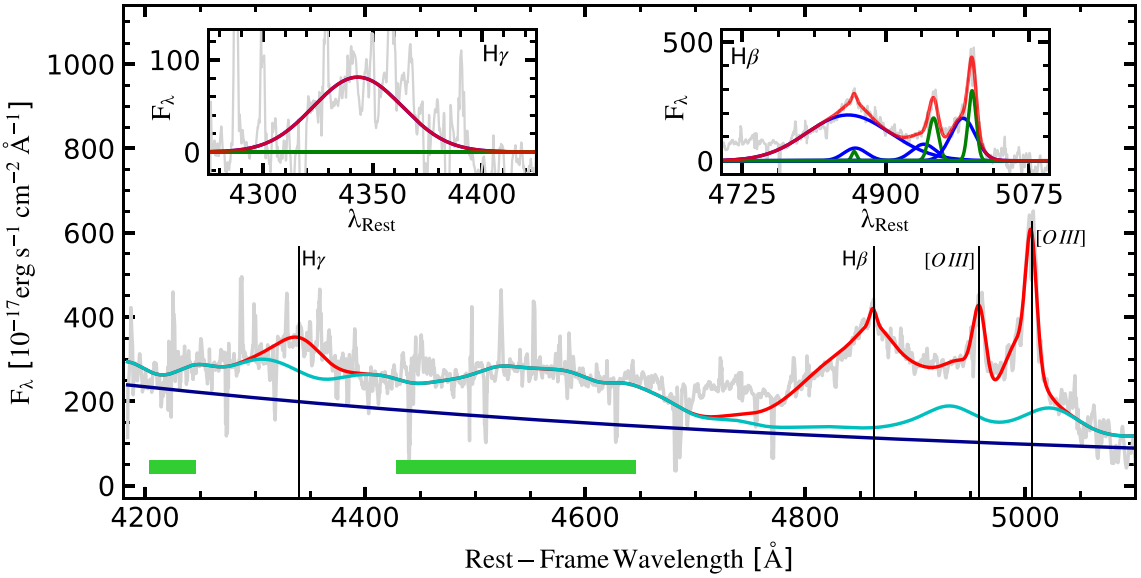

Figure 6. We present the H-band spectrum for ULASJ2315+0143 with a dust correction, $E(B-V)^{\rm QSO} = 1.55$, applied in grey. The continuum is presented in navy blue, and the windows over which the continuum was fitted are denoted by the thick, lime-green lines. In addition, the combination of the continuum and iron template are presented in teal. The final fit of the spectrum is presented in red. Noteworthy emission lines are marked by thin black lines and labelled appropriately. The smaller panels are labelled by the line/complex they represent. The continuum subtracted total fit is presented in red, the broad components contributing to the total fit are presented in blue and finally, the narrow components are presented in green.

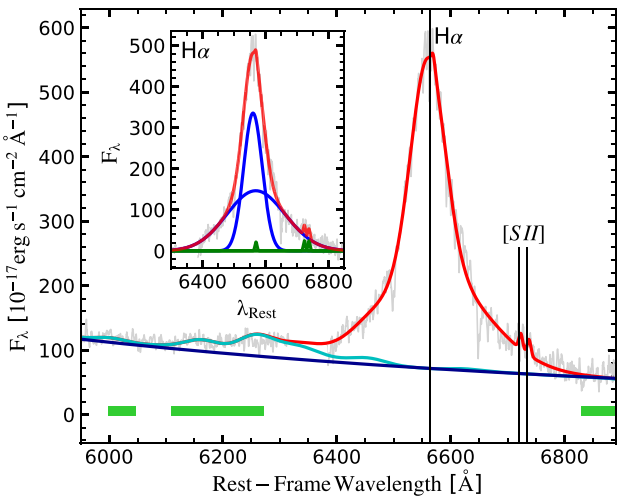

Figure 7. Same as Fig. 6, but instead we present the K-band spectrum.

Table 3. Quasar emission line properties inferred from the ULASJ2315+0143 X-Shooter spectrum. Since the [O II] emission was used to determine $z_{\rm sys}$, its V50 velocity is zero by definition.

Species	S/N	REW (Å)	FWHM (km s^{-1})	V50 (km s^{-1})
Lyα	254	97±2	1070±10	−350±20
N V	11.9	16±1	4227±3	−930±210
O IV/Si IV	4.3	7.0±0.3	5773±6	−940±160
C IV	16.1	24±1	3900±390	−1080±110
O II	12.8	8±2	330±120	0
Hγ	2.5	21±1	3340±190	+60±20
Hβ	23.9	230±30	6030±580	−120±50
O III	37.0	68±12	940±80	−380±90
Hα	42.8	820±10	4040±70	−320±30

Notes. Here, the results pertaining to the [O III] emission refer to the λ5008 Å line.

of the Hβ emission using the following equation (Vestergaard & Peterson 2006):

$$\log(\mathrm{H}\beta, \mathrm{M_{BH}}[\mathrm{M}_\odot]) = \log\left\{\left[\frac{\mathrm{FWHM(H}\beta)}{1000\,\mathrm{km\ s^{-1}}}\right]^2\left[\frac{\lambda \mathrm{L}_\lambda(5100\,\text{Å})}{10^{44}\,\mathrm{erg\ s^{-1}}}\right]^{0.50}\right\} + (6.91 \pm 0.02), \quad (4)$$

where $\lambda \mathrm{L}_\lambda(5100\ \text{Å}) = 10^{47.51}\,\mathrm{erg\ s^{-1}}$ is the continuum luminosity of ULASJ2315+0143 evaluated at 5100 Å, using the best-fitting continuum from PYQSOFIT in the H band. Equation 4 yields $\log_{10}(\mathrm{H}\beta, \mathrm{M_{BH}}[\mathrm{M}_\odot]) = 10.26 \pm 0.05$, consistent with the analysis of a much shorter exposure SINFONI spectrum of this target in Banerji et al. (2015). Using the FWHM correction between Hβ and Hα detailed in Greene & Ho (2005), we can also estimate $\mathrm{M_{BH}}$ from the Hα emission, yielding $\log_{10}(\mathrm{H}\alpha, \mathrm{M_{BH}}[\mathrm{M}_\odot]) = 10.17 \pm 0.09$. The uncertainties in $\lambda \mathrm{L}_\lambda(5100\ \text{Å})$ were calculated by generating 500 simulated spectra perturbed with Gaussian noise consistent with the noise spectrum and implementing PYQSOFIT after each iteration. Uncertainty estimates in $\mathrm{M_{BH}}$ were then calculated by propagating the uncertainty in the continuum luminosity through equation (4), drawing the normalization constant from a Gaussian distribution with $\mu = 6.91$ & $\sigma = 0.02$. This does, however, neglect the large (∼0.5 dex) systematic uncertainties reported in single-epoch $\mathrm{M_{BH}}$ estimates by Vestergaard & Peterson (2006). Previous estimates of the dynamical mass of this system based on CO(3-2) observations suggest $\log_{10}(\mathrm{M_{dyn}}/\mathrm{M}_\odot) \simeq 11$ (Banerji et al. 2021). The SMBH in ULASJ2315+0143 is therefore overmassive with respect to the host galaxy but broadly consistent with the scaling relation for high-redshift luminous quasars (e.g. Pensabene et al. 2020).

Using the relation between $\mathrm{L}_\lambda(5100\,\text{Å})$ and $\mathrm{L_{Bol}}$ from Netzer (2019) we define a bolometric correction $\mathrm{BC}_{5100} = 4.46$, yielding $\mathrm{L_{Bol}} = 10^{48.16}\,\mathrm{erg\ s^{-1}}$ for ULASJ2315+0143. Using this bolometric luminosity and our estimate of the black-hole mass

Downloaded from https://academic.oup.com/mnras/article/533/3/2948/7733827 by guest on 07 November 2024

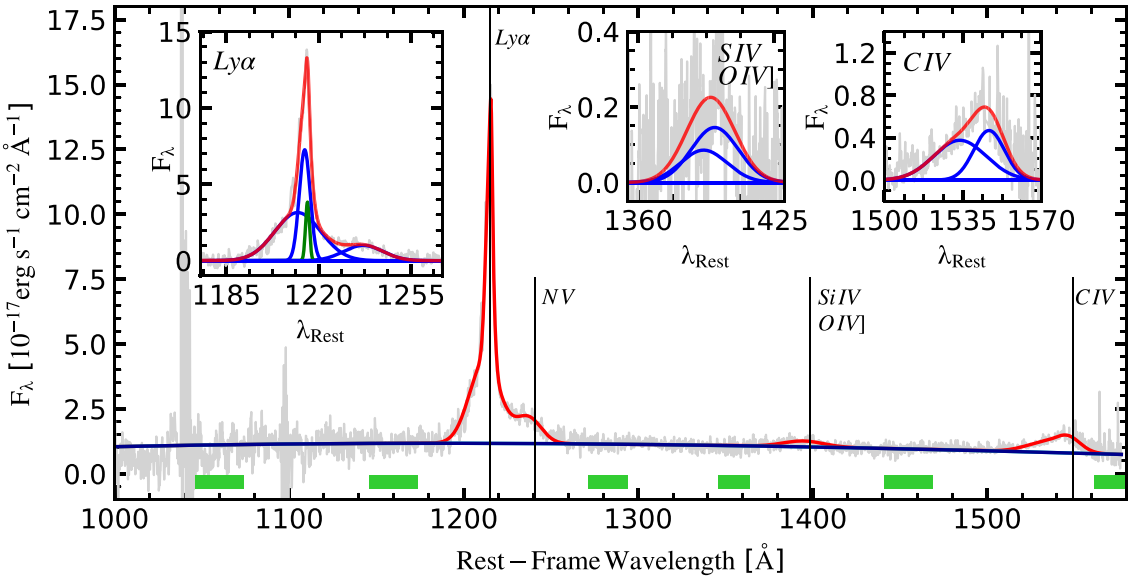

Figure 8. Same as Fig. 6, but instead we fit the UVB spectrum without a dust correction applied.

yields an Eddington-scaled accretion rate of $\log_{10}(\lambda_{\rm Edd}) = -0.19$. Given the intrinsic X-ray luminosity $L_{\rm X,int} = 10^{45.6}$ erg s^{-1} for ULASJ2315+0143 (Lansbury et al. 2020), the corresponding X-ray bolometric correction $\log_{10}(k_{\rm Bol}, L_{\rm X}) = 2.56$. While this is extreme, X-ray bolometric corrections as large as $k_{\rm Bol,X} = 100-1000$ have already been observed in the *WISE*/SDSS selected hyperluminous (WISSH) quasar sample with bolometric luminosities $L_{\rm Bol} > 2 \times 10^{47}$ erg s^{-1}. Indeed, the inferred X-ray bolometric correction is consistent with the trends in bolometric correction with both black-hole mass and Eddington-scaled accretion rate inferred in other hyperluminous infrared-selected quasar populations (Martocchia et al. 2017). Similarly, the mid-infrared luminosity inferred from *Wide-field Infrared Survey Explorer* (*WISE*) photometry, $\log_{10}(L_{6\mu m}) = 47.5$, suggests a mid-infrared bolometric correction $\log_{10}(k_{\rm Bol}, L_{6\mu m}) = -0.66$. This is consistent with the $\log_{10}(k_{\rm Bol}, L_{7.8\mu m}) = -0.35 \pm 0.4$ reported amongst blue AGN (Weedman et al. 2012).

3.3.3 *UV emission- and absorption-line features*

In Section 3.2, we concluded that the broad emission lines seen in the UVB can be explained by a scattered or leaked quasar component. Hence, we do not apply any dust correction to the UVB spectrum before fitting the lines using PYQSOFIT. We model three main broad-line complexes in the UVB. We parametrize the Lyα/N V complex with four Gaussians, one broad component attributed to the N V contribution and the remainder attributed to the Lyα contribution. The Si IV/O IV] complex is modelled by two broad components and so too is the C IV emission. To enable a more robust reconstruction of the emission line profile, narrow absorption features must first be masked. We adopt an iterative approach for this. First, we fit the raw spectrum with PYQSOFIT, the result of which serves as a pseudo-continuum for subsequent fits. Pixels whose flux $> 2\sigma$ below the pseudo-continuum are replaced by the corresponding flux element in the pseudo-continuum itself. The process is then repeated until successive models converge (in this case, five iterations were sufficient). The results are presented in Fig. 8 and the emission-line properties are summarized in Table 3.

In Fig. 8, the C IV emission line appears broad, blueshifted, and of modest EW. These C IV properties are typical of those found in luminous, blue, Type 1 QSOs and have been associated with BLR winds along certain sight-lines (Richards et al. 2011; Rankine et al. 2020; Stepney et al. 2023; Temple et al. 2023). The N V emission is also blueshifted. As N V has a similar ionizing potential to C IV, the two species are likely emitting from similar regions in the BLR, hence, the broadly consistent line properties are to be expected. Conversely, the Lyα EW is uncharacteristically large in comparison to N V. The velocity off-set of the narrow component of the Lyα emission (green Gaussian in top left panel of Fig. 8) is –16±170 km s^{-1}, consistent with the uncertainties on the systemic redshift. We measure a line ratio N V/Lyα ~ 0.16 for ULASJ2315+0143, significantly less than the N V/Lyα ~ 0.31 observed in blue Type 1 QSOs (Shen 2016). We propose that the line profile can be explained either by a contribution from a star-forming galaxy (as discussed in Section 3.2) or some scattering of the quasar light. For a full discussion see Section 4.1.

We searched for absorption features associated with a number of high-ionization species in the UV spectrum as follows. First, the spectrum is renormalized by a pseudo-continuum defined by the best PYQSOFIT broad emission line model (Fig. 8, red). We then employ a cross-correlation technique similar to that described in Hewett & Wild (2010), Rankine et al. (2020), and Stepney et al. (2023). Our default model is defined as $F/F_{\rm cont} = 1$. We then define a grid of Gaussian absorption line models with various line depths and widths (the narrowest model explored has width $\sigma \sim 30$ km s^{-1} – equal to the resolution of X-Shooter in the UVB arm). For doublets, the linewidths and line off-sets are tied and we additionally explore the following line ratios: 1:3, 1:2, 2:3, and 1:1. The best model parameters and corresponding cross-correlation value are recorded at each line off-set. The absorption-line model whose combination of off-set, depth, width and line ratio yields the maximum cross-correlation value is added to the default model and the process is then repeated. If the best absorption model does not represent a $>4\sigma$ improvement in cross-correlation value over the default model or the

Downloaded from https://academic.oup.com/mnras/article/533/3/2948/7733827 by guest on 07 November 2024

Table 4. Summary of different velocity components of narrow associated absorption-line systems (AALs) shown in Fig. 9.

Species	Component	Offset (km s^{-1})
C IVλλ1548.19, 1550.77	2	−565
	3	−348
	5	871
Si IVλλ1393.76, 1402.77	1	−2050
	3	−313
N Vλλ1238.82, 1242.80	3	−360
Si IIIλ1206.52	3	−311
	4[a]	385

[a]Potentially blueshifted H I absorption, $V_{\rm off-set} = -1870$ km s^{-1}. *Notes.* Velocity offsets are relative to the [O II] systemic redshift. We group velocity components whose off-sets are consistent within the uncertainty on $z_{\rm sys}$

new absorption feature does not exceed a signal-to-noise of three (S/N > 3), the new absorption line model is rejected and the search is complete.

The results are summarized in Table 4 and Fig. 9. Five distinct velocity components are detected, with component 3 at $v \simeq -340$km s^{-1} detected in all species, suggestive of outflowing gas at a range of ionization parameters. The absorption in C IV at this velocity is saturated, suggesting a high covering fraction of C IV gas. In other species, such as N V and Si IV, the covering fraction of the gas is much lower. We also see additional absorption components in C IV at velocities of ≃–565 and ≃ + 871 km s^{-1} that are not present in N V or Si IIIλ1206.52 and Si IV, and have a lower covering fraction relative to the –340 km s^{-1} component. Furthermore, we observe a very high-velocity component in the Si IV absorption, with a velocity ≃–2050 km s^{-1}. We also note that the redshifted Si IIIλ1206.52 component at +385 km s^{-1} could conceivably also represent blueshifted Lyα absorption.

4 DISCUSSION

4.1 Source of the UV emission

In Section 3.2, we concluded that a simple dust-attenuated Type 1 QSO SED model is unable to reproduce the emission blueward of ∼ 4000 Å in ULASJ2315+0143 and that emission from a secondary blue AGN component and/or a star-forming host galaxy likely contributes in this region. We now further explore the origin of the excess UV emission.

4.1.1 A dual AGN system?

Could the blue AGN component seen in the X-Shooter spectrum of ULASJ2315+0143 be consistent with the presence of a second AGN in the system, which is more than 1000 times fainter in the UV than the primary dusty quasar? ULASJ2315+0143 is hosted in a major merger based on the ALMA observations reported in Banerji et al. (2021). The two galaxies in the merger are both detected in CO(3-2) and are separated by ∼15 kpc in projection. During galaxy mergers, when both of the SMBHs are activated, a dual quasar could be formed (Begelman, Blandford & Rees 1980). Observations over the past decades have reported hundreds of dual quasars with redshifts from local to $z = 5.66$ (Yue et al. 2021), and separations from Mpc scale down to 230 pc (Koss et al. 2023). Therefore, a secondary quasar could be a plausible source of the UV emission.

If a secondary AGN is present, however, it is likely not associated with the companion merging galaxy detected in CO with ALMA. The merging companion galaxy has gas excitation conditions that are more typical of star-forming galaxies rather than AGN as well as narrower molecular emission lines compared to the quasar host (Banerji et al. 2018), all of which seems to suggest no actively accreting black hole in this galaxy. Moreover, the image decomposition presented in Fig. 2 suggests the presence of at most a single point-source contributing to the UV emission, located at the centroid of the primary quasar host rather than the merging companion. If this is a dual AGN system, then the separation between the secondary AGN and the quasar host galaxy must therefore be less than the typical seeing of the HSC images (0.6 arcsec, or 4.8 kpc at $z = 2.566$). The observational constraints of dual fractions at this separation are still poor, due to the limited resolution (e.g. Silverman et al. 2020). On the other hand, Steinborn et al. (2016) studied the statistics and properties of closely separated (<10 kpc) dual AGN at $z = 2$ in the Magneticum simulation. This cosmological simulation encloses a volume of 182 Mpc^3 and produces 35 BH pairs, among which nine are dual AGN. Thus, the spatial density of dual AGN is ∼0.05 Mpc^{-3}. They also report that the dual fraction (the ratio of the number of dual AGN and the total number of AGN) is 1.2 ± 0.3 per cent in the simulation (also see Volonteri et al. 2016; Rosas-Guevara et al. 2019, this fraction varies roughly between 0.1 and 5 per cent). Therefore, the dual AGN scenario, although cannot be fully ruled out, is statistically unlikely.

4.1.2 Leaked or scattered light from the primary quasar?

Since the AGN emission is unlikely to originate from a secondary source, the broad UV emission most likely originates from the primary quasar. Here, we will discuss two potential scenarios – (i) leaked AGN emission, escaping through 'windows' in a patchy dust morphology and (ii) scattered AGN emission.

In Section 3.2, we show that when modelling the rest-frame UV portion of the SED with an unattenuated AGN component, just 0.05 per cent of the intrinsic quasar emission is required to reproduce the continuum. Since the UV continuum is consistent with the shape of a blue AGN, we require a consistent covering factor across all wavelengths to preserve the shape of the accretion disc's multitemperature black-body in a 'leaked' light scenario. For such a small fraction of the intrinsic radiation to be observed, we would require the obscuring medium to populate the extremely local regions of the AGN. The required dust morphology is then extremely contrived and hence we conclude that leaked AGN emission through a patchy obscuring medium is an unlikely cause of the UV-excess (Assef et al. 2015).

An alternative scenario is that AGN emission is scattered towards the line of sight by the obscuring medium. This is the favoured explanation in HotDOGs, where broad-band UV photometry confirms that the emission is linearly polarized, having been scattered from ionized gas (Assef et al. 2015, 2020, 2022). However, unlike HotDOGs and ERQs, ULASJ2315+0143 shows evidence of high-ionization line blueshifts in the rest-frame UV emission (see Fig. 8 and Table 3). While this does not completely rule out the scattered light scenario, it does limit the number of feasible dust geometries.

Should the obscuring medium be distant enough such that the incident AGN emission features only the sight lines with blueshifted high-ionization lines, the scattered spectrum could also exhibit blueshifts. A candidate for the obscuring medium is then some kind of dusty toroidal structure outside the BLR. In Fig. 10, we show the infrared photometry of ULASJ2315+0143 from UKIDSS and *WISE* compared to the best-fitting SED from Section 3.2. The

Downloaded from https://academic.oup.com/mnras/article/533/3/2948/7733827 by guest on 07 November 2024

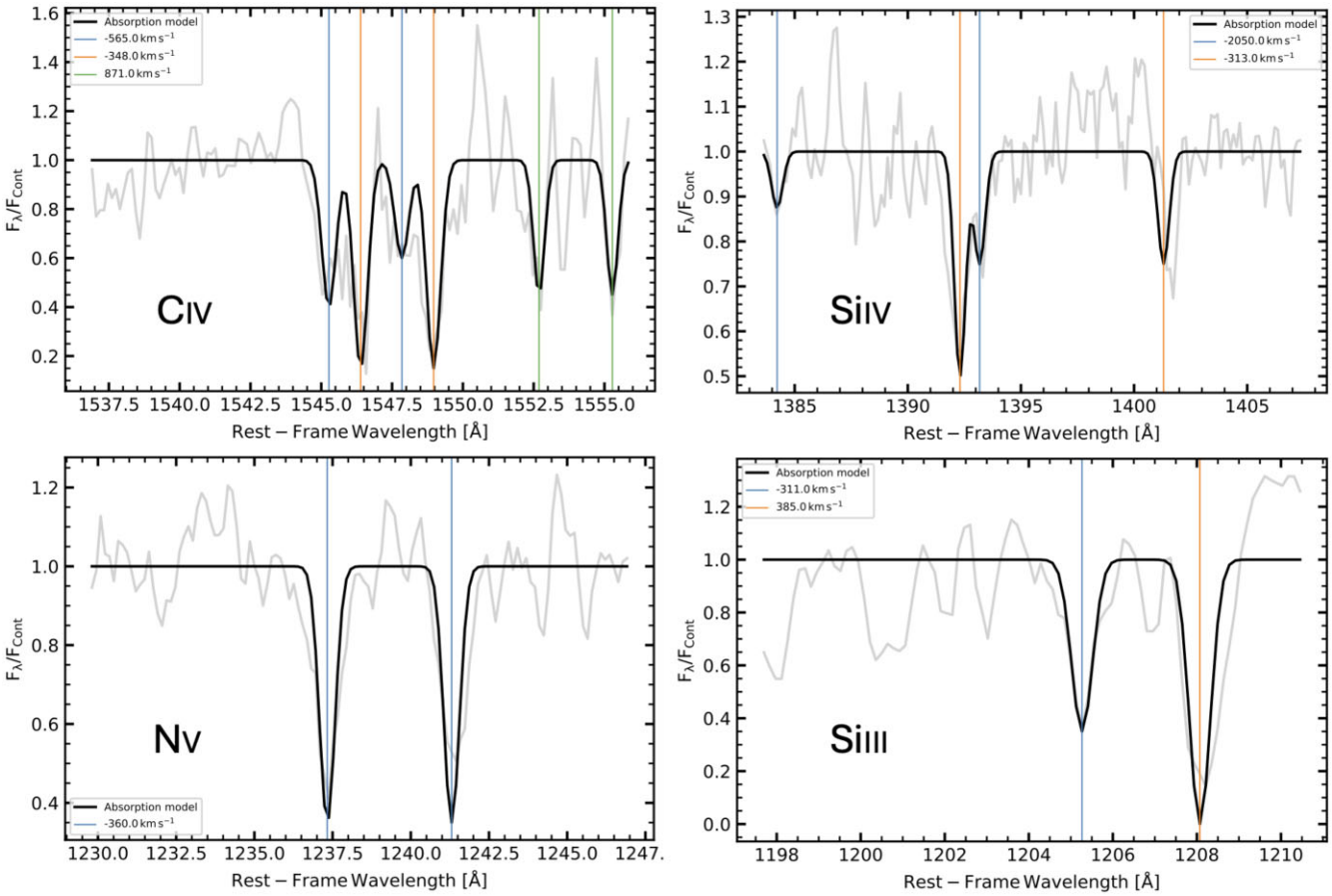

Figure 9. The UVB narrow absorption line features detected in the X-Shooter spectrum. The flux density normalized by the PYQSOFIT pseudo-continuum is presented in grey. The absorption model reconstructions are presented in black. The species are labelled in each panel. We mark the various velocity components with vertical lines in each panel.

infrared emission in the SED model represents the average infrared SED for an SDSS quasar at $z \sim 2$ (Temple et al. 2021a) with a hot dust temperature of $T_{bb} = 1243$ K and a hot dust normalization – defined as the ratio between the hot dust and accretion disc luminosities at 2 μm – $L_{2\mu m,Dust}/L_{2\mu m,QSO} = 2.5$. We can immediately see that this SED model is inconsistent with the photometry of ULASJ2315+0143 when extrapolated to mid-infrared wavelengths. A value of $L_{2\mu m,Dust}/L_{2\mu m,QSO} = 0.5$, however, is better able to match the observed photometry. The flux density observed in the $W4$ band (not shown in Fig. 10) is $10^{-17.1\pm0.1}$erg s^{-1} cm^{-2} Å^{-1}. The mid-infrared SED therefore remains flat to a rest-frame wavelength $\sim 6\mu m$ (corresponding to a dust temperature of ~ 450K). We therefore conclude that the ratio between the hot dust and accretion disc luminosities in ULASJ2315+0143 is significantly lower than observed in blue quasars (see Temple et al. 2021a).

The absence of hot dust emission on typical torus scales could suggest that the obscuring medium responsible for the significant ($E(B-V)^{QSO} = 1.552$ mag) extinction towards the quasar continuum is likely on ISM, rather than nuclear scales. Alternatively, self-absorbed cold torus models have been invoked to explain flatter mid-infrared SEDs (e.g. Hönig 2019). However, we might expect a more symmetrical line profile in C IV, with weaker blueshifts should the scattering medium lie primarily on nuclear scales close to the quasar BLR. Hence, we favour the depleted torus scenario, proposing a plausible geometry for ULASJ2315+0143 in Fig. 11. A more complete analysis of the mid-infrared SEDs of the HRQ population is deferred to future work. In Fig. 11, the excess UV emission seen in the spectrum is traced by dashed black arrows. We show multiple sight-lines originating from the accretion disc scattered by interstellar dust towards the observer.

4.1.3 Associated absorption-line systems in ULASJ2315+0143

In Fig. 9, we can see numerous narrow absorption features in the rest-frame UV spectrum with linewidths of a few hundred km s^{-1} and that lie within 3000 km s^{-1} of the quasar systemic redshift. These properties are consistent with the associated absorption line (AAL) systems that have been detected in the spectra of numerous luminous quasars (e.g. Vanden Berk et al. 2008; Hamann et al. 2011; Shen & Ménard 2012; Chen et al. 2018). AALs can have a wide range of origins tracing gas in quasar inflows and outflows, in the halos of the quasar host galaxy or indeed gas reservoirs on circumgalactic scales (Foltz et al. 1986; Tripp, Lu & Savage 1998). Statistical studies suggest that most AALs are intrinsic to the quasars, and hence can serve as important probes of the quasar environment (Nestor, Hamann & Rodriguez Hidalgo 2008; Wild et al. 2008). As such, the detection of significant absorption in this gas-rich merger is perhaps not surprising. Dust-reddened quasars in the SDSS have been associated with a higher incidence of AALs (Richards et al. 2003; Vanden Berk et al. 2008) and 2MASS red quasars with a higher incidence of broad absorption line (BAL) features (e.g. Urrutia et al. 2009). However, to our

Downloaded from https://academic.oup.com/mnras/article/533/3/2948/7733827 by guest on 07 November 2024

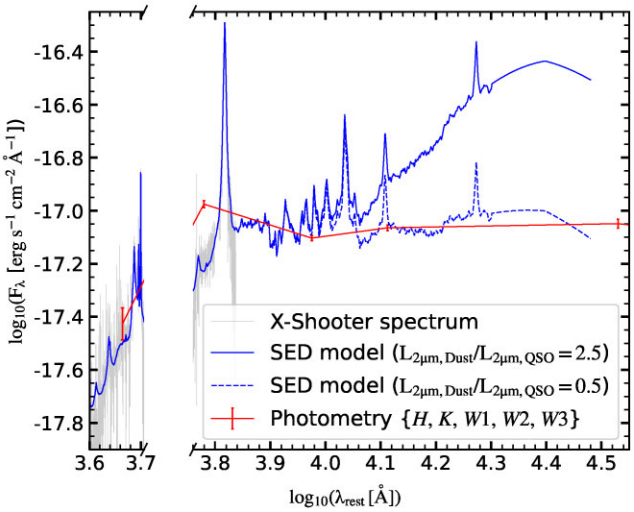

Figure 10. The X-Shooter spectrum of ULASJ2315+0143 is presented in grey, with the broad-band photometry from UKIDSS and WISE overlaid in red. The best-fitting UV/optical SED, see Section 3.2, is extrapolated to mid-infrared wavelengths (blue, solid), assuming $L_{2\mu m,Dust}/L_{2\mu m,QSO}$ = 2.5. The photometry is inconsistent with the SED model redward of the $W1$ filter. The same SED model assuming $L_{2\mu m,Dust}/L_{2\mu m,QSO}$ = 0.5 (blue, dashed) is more consistent with the photometry. Both SED models assume a hot dust temperature of 1243K. This suggests that the ULASJ2315+0143 system contains less hot dust than the typical blue SDSS quasar, where $L_{2\mu m,Dust}/L_{2\mu m,QSO} \gtrsim 1.0$ (Temple et al. 2021a).

knowledge, our study represents the first detection of multiple AAL systems in a quasar with such extreme dust reddening of $E(B-V) > 1.5$.

The most prevalent absorption feature detected in multiple species is at a velocity of ∼–340 km s^{-1} relative to systemic. The higher ionization gas at –340 km s^{-1} could conceivably be associated with the merging companion, which is located 15 kpc away in projected distance from the quasar and blueshifted in CO(3-2) emission by 170 km s^{-1} relative to the quasar (Banerji et al. 2021). However, the high-ionization gas is most likely located closer to the ionizing source, effectively shielding the lower ionization gas, which is likely spatially co-incident with the warm molecular gas traced by CO(3-2). We also detect redshifted AALs at velocities of ≃385 and ≃870 km s^{-1}. These components may be associated with the CO(1-0) cold gas reservoir in this quasar, which is off-set in velocity by ≃500 km s^{-1} (Banerji et al. 2018). The cold gas reservoir is also very spatially extended on projected scales of ∼50 kpc. The geometry of the system showing the different spatial scales for the gas potentially producing the AAL features is shown in Fig. 11.

4.1.4 Star-forming host

As discussed in Section 3.2, HSC imaging is suggestive of a host galaxy contribution to the rest-frame UV flux. This is also consistent with the strong nebular emission observed in Lyα and [O II] as well as the presence of multiple narrow absorption line systems in Fig. 9 which could conceivably be associated with the gas in the quasar host galaxy. The $SFR_{FUV} \sim 3 \times SFR_{[O\,II]}$. The unobscured SFR, predicted by the far-infrared and submillimeter continuum emission, for this source is $SFR_{FIR} = 680 \pm 100\,M_\odot\,yr^{-1}$ (Banerji et al. 2018). Main-sequence galaxies at similar redshifts and A_V^{Gal}, report similar SFR_{FIR} to ULASJ2315+0143 , with their average $SFR_{H\alpha,obs} = 20 M_\odot\,yr^{-1}$ consistent with our own estimate of the SFR from [O II] (Puglisi et al. 2017). Given SFR_{FUV}, $SFR_{[O\,II]}$ and $SFR_{H\alpha,obs}$ estimates make similar assumptions regarding the dust extinction, it would be reasonable to conclude that the [O II] estimate is less than the FUV estimate for ULASJ2315+0143 because the rest-frame UV continuum emission in this source does not originate purely from a star-forming host galaxy but rather has some contribution from scattered AGN light as discussed above.

4.2 Multiphase winds in ULASJ2315+0143

In this section, we discuss the line properties of ULASJ2315+0143 in the context of AGN-driven winds as well as drawing comparisons to observations from other QSO populations.

There exists a relationship between BLR outflows, as probed by the C IV blueshift, and both M_{BH} and Eddington-scaled accretion rate in blue quasars. This relationship is evident in both simulations (e.g. Giustini & Proga 2019) and observations of blue Type 1 SDSS quasars up to $z_{sys} \sim 4$ (e.g. Stepney et al. 2023; Temple et al. 2023). The dependence of C IV blueshift on the M_{BH}-λ_{Edd} plane tells us how BLR outflows are linked to the accretion physics of QSOs. For significant (> 1000 km s^{-1}) C IV blueshifts, quasars require $\lambda_{Edd} > 0.2$ and $M_{BH} > 10^9 M_\odot$. Our observations of ULASJ2315+0143 are consistent with this picture, with a relatively strong C IV blueshift, V50 = 1075km s^{-1}, owing to the large SMBH mass, $M_{BH} = 10^{10.26} M_\odot$, and Eddington-scaled accretion rate, $\log_{10}(\lambda_{Edd}) = -0.19$. Fundamentally, this suggests that the dependence of BLR outflow velocities on black hole mass and accretion rate is broadly similar in blue and HRQs.

Moving to kpc-scales, we can probe NLR winds with the [O III] emission line W80 (e.g. Coatman et al. 2019; Perrotta et al. 2019; Temple et al. 2019; Villar Martín et al. 2020). In Fig. 12, we compare the BLR and NLR wind velocities of ULASJ2315+0143 to a sample of blue QSOs Temple et al. (2024) and show that ULASJ2315+0143 appears consistent with the trend observed in optically selected quasars. While ULASJ2315+0143 shows evidence of significant NLR winds, as probed by [O III] W80, the object is not extreme. This picture is consistent with the BLR winds as probed by C IV blueshift. Since the winds in both the BLR and NLR are similarly moderate, a common mechanism could be responsible for the gas velocities at these different scales.

In addition, we can harness the [O III] emission to investigate the energetics of the outflowing ionized gas. By assuming a symmetric biconical geometry and that the emitting clouds have the same density, Cano-Díaz et al. (2012) derive the following expression for the mass-loss rate of the NLR outflow:

$$\dot{M}_{out}^{ion} = 164\,\frac{L_{44}([O\,III])\,V_3}{\langle N_{e3}\rangle\,10^{[O/H]}\,R_{kpc}}\,M_\odot\,yr^{-1}, \quad (5)$$

where $L_{44}([O\,III])$ is the broad [O III] line luminosity in units 10^{44} erg s^{-1}, V_3 is the outflow velocity in units of 1000 km s^{-1}, $\langle N_{e3}\rangle$ is the NLR outflow electron density in units of 1000 cm^{-3}, $10^{[O/H]}$ is the oxygen abundance in solar units and R_{kpc} is the radius of the outflowing region in units of kpc. Given the uncertainty in the amount of dust attenuation affecting the NLR, we use the measured [O III] luminosity from the spectrum before any dust correction is applied. The kinetic power associated with the outflow is then given by the following equation:

$$\dot{\epsilon}_k^{ion} = 5.17 \times 10^{43}\,\frac{C\,L_{44}([O\,III])\,V_3^3}{\langle N_{e3}\rangle\,10^{[O/H]}\,R_{kpc}}\,erg\,s^{-1}, \quad (6)$$

where $C = \langle N_{e3}\rangle^2/\langle N_{e3}^2\rangle \approx 1$. As in Perrotta et al. (2019), we assume that since the [O III] emission is not core dominated in

Downloaded from https://academic.oup.com/mnras/article/533/3/2948/7733827 by guest on 07 November 2024

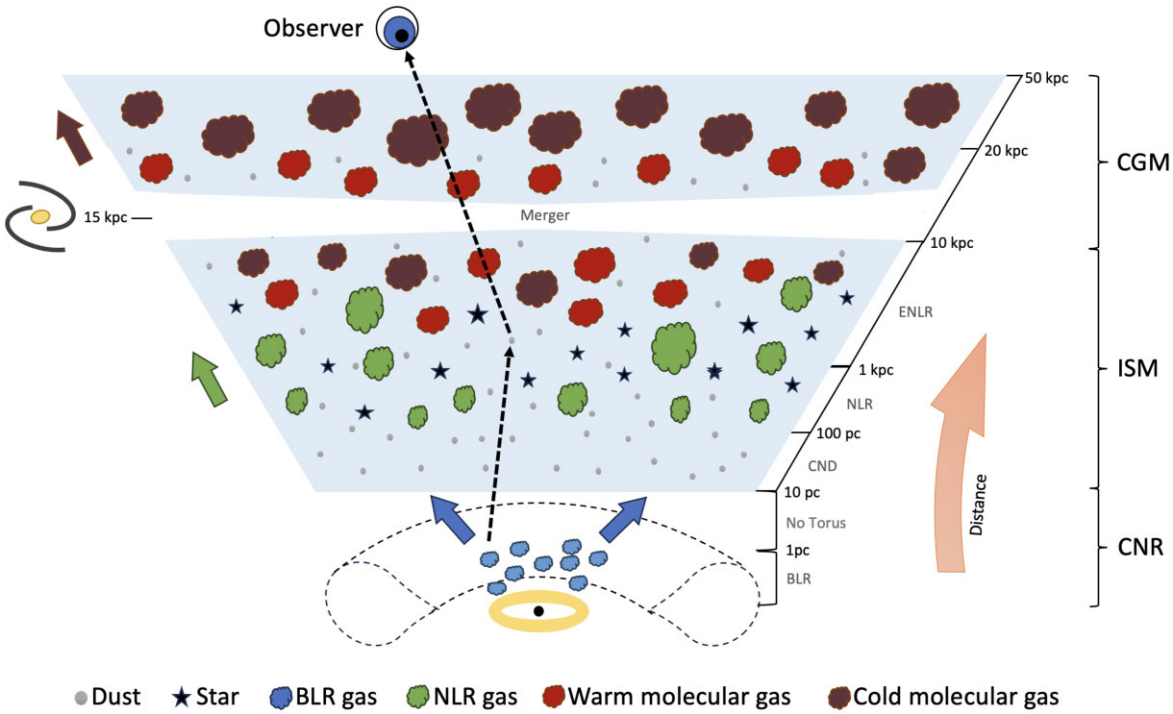

Figure 11. An illustration of our proposed geometry that best describes ULASJ2315+0143 focusing on the different scales associated with different features in the X-Shooter spectrum and the multiwavelength observations of this source. On sub-pc scales, we illustrate the BLR gas with blue clouds. Since the mid-infrared SED is devoid of hot dust (Fig. 10), we illustrate the missing/depleted torus with dotted black lines stretching to ∼10 pc. ALMA observations suggest that the ISM dust is on scales of ∼15–20 kpc based on the size of the millimetre continuum emission. NLR gas and star-forming regions are represented with green clouds and black stars, respectively. The warm molecular gas is depicted with red clouds and the cold molecular gas is depicted with maroon clouds. A cartoon sight line, scattered from ISM dust and then subsequently absorbed by the warm and cold gas reservoirs, potentially giving rise to the AAL features in the UV spectrum, is illustrated by the dashed black arrow. The merging companion galaxy resides at 15 kpc and is illustrated to the left of the sketch. Blue, green, and maroon arrows represent BLR, NLR, and cold molecular gas flows, respectively, all of which exhibit significant velocity offsets relative to the systemic redshift.

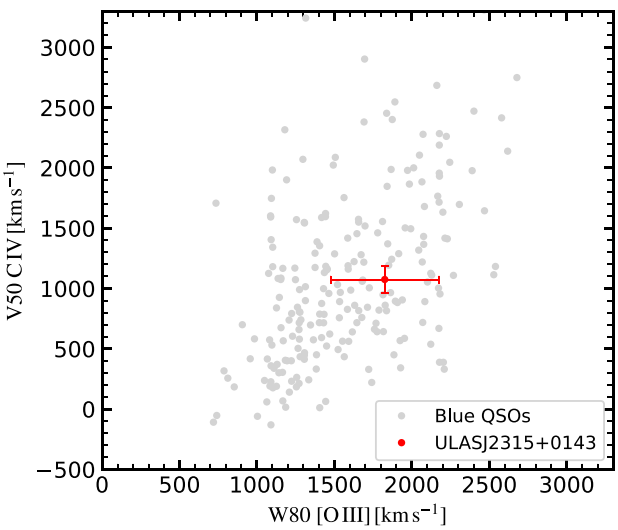

Figure 12. The C IV emission line centroid [O III] W80 relation for a sample of blue SDSS quasars (Temple et al. 2024) are presented in grey. ULASJ2315+0143 , presented in red, shows evidence of significant (though not extreme) BLR and NLR winds, consistent with the trend observed in blue SDSS quasars.

ULASJ2315+0143 , $V_{98} = 2521\,\mathrm{km\,s^{-1}}$ serves as a good indicator for the outflow velocity and adopt solar metallicities. Using the line ratios between the narrow and broad components of [O III] (Fig. 6), we attribute ∼ 75 per cent of the total line luminosity to the broad outflow component. Bischetti et al. (2017) find that amongst the WISSH broad-line quasar sample $\langle N_{e3}\rangle \sim 200\mathrm{cm}^{-3}$ and the [O III] emission regions are extended to 1–7 kpc. Since we have no spatially resolved data for the [O III] emission in ULASJ2315+0143 at present, we adopt the 4 kpc threshold for strong [O III] winds reported in another HRQ from our sample in Banerji et al. (2012) – ULASJ1002+0137 – which was observed by Veilleux et al. (2023). Applying these assumptions to equations (5) and (6) yields $\dot{M}^{\mathrm{out}}_{\mathrm{ion}} = 199\,\mathrm{M_\odot\,yr^{-1}}$ and $\dot{\epsilon}^{\mathrm{ion}}_{k} = 10^{44.61}\mathrm{erg\,s^{-1}} \sim 0.001\,\mathrm{L_{Bol}}$.

Our estimate for the kinetic power of the ionized gas outflows is consistent with the blue quasars presented in Shen et al. (2011), given the bolometric luminosity of ULASJ2315+0143 , however, they seems relatively weak when compared to the ERQs presented in Perrotta et al. (2019). It is important though to be mindful of the different assumptions made in the kinetic power estimates of the two samples. First, in ERQs the entire [O III] line luminosity is attributed to the outflow whereas we attribute ∼ 75 per cent of the total line luminosity to the broad outflow component based on our line fits. Secondly, Perrotta et al. (2019) adopt $R_{\mathrm{kpc}} = 1$ since two of their ERQ's [O III] emission regions are spatially unresolved down to a resolution of ∼ 1.2 kpc by the W.M. Keck Observatory OSIRIS integral field spectrograph significantly smaller than our assumption

Downloaded from https://academic.oup.com/mnras/article/533/3/2948/7733827 by guest on 07 November 2024

of 4 kpc. Both of these assumptions are likely to overestimate the kinetic power of the outflows by a factor of several relative to our assumptions. In addition, if we assume the colour $[i - W3_{\rm Vega}]$ is a good indicator of the dust extinction in these systems ($[i - W3_{\rm Vega}] \sim 7.78$ for ULASJ2315+0143), ULASJ2315+0143 suffers more extinction than the average ERQ. Hence, the [O III] line luminosity may be more attenuated in ULASJ2315+0143 , resulting in an underestimate of the kinetic power when compared to the ERQ sample. Neither estimate corrects the observed [O III] luminosity for dust extinction. Given these assumptions, the ionized outflows observed in ULASJ2315+0143 are likely similar to those observed in ERQs in terms of mass-loss rate and kinetic power.

4.3 Comparison to *JWST* little red dots

Recent *JWST* observations point to a significant population of LRDs at $z_{\rm sys} \gtrsim 5$ with blue rest-frame UV photometric colours – for example, Kocevski et al. (2023), Onoue et al. (2023), Greene et al. (2024), and Kocevski et al. (2024). While the true nature of some sub-samples of LRDs is still debated (e.g. Matthee et al. 2024), 60 per cent of the objects from the UNCOVER field show definitive evidence of broad (FWHM > 2000 km s^{-1}) Hα emission and are hence classified as dust-reddened AGN (Greene et al. 2024). Here, we consider whether ULASJ2315+143 is a cosmic-noon analogue of this sample of *JWST*'s LRDs – effectively a big red dot at $z \sim 2.5$.

Some SED models suggest that the photometry of these dusty AGN is best-fit by the combination of a dust-attenuated AGN and a massive star-forming galaxy (e.g. Pérez-González et al. 2024), whereas others prefer a scattered light scenario as in ULASJ2315+0143 (e.g. Williams et al. 2024). The inferred rest-frame UV luminosities of LRDs are significantly fainter than that of UV-selected AGN at similar epochs ($-20 < {\rm M_{UV}} < -16$), consistent with a less-than-one per cent scattering of the accretion disc emission, similar to ULASJ2315+0143 (Greene et al. 2024). However, unlike the X-ray luminous ULASJ2315+0143 , only 2/341 LRDs are detected in the X-ray. The two X-ray-confirmed LRDs show evidence of relatively high column densities, $\log_{10}(N_{\rm H}\,[{\rm cm}^{-2}]) \sim 23$, consistent with ULASJ2315+0143 and other HRQs. One interpretation for the absence of X-ray detections across the rest of the sample is that LRDs generally have denser gas columns with higher covering fractions than typically observed in HRQs, with the high column densities of neutral hydrogen extending to ISM scales (Kocevski et al. 2024). Furthermore, Greene et al. (2024) propose that prolonged episodes of super-Eddington accretion could explain why LRDs are X-ray weak when compared to their optical luminosities. However, without large-scale spectroscopic confirmation it is still possible that some LRDs are starburst galaxies. Strikingly, the mid-infrared photometry of a sub-sample of LRDs show evidence of remarkably flat mid-infrared emission (Williams et al. 2024). One interpretation for the absence of hot (>1000 K) dust emission is that these objects are not in fact AGN, and instead the mid-infrared photometry is tracing the continuum from stellar populations whose spectrum peaks at $\sim 0.5-3$ μm in the rest frame (Sawicki 2002). However, since we also observe a similar flattening of the mid-infrared SED in ULASJ2315+0143 and other HRQs, we propose an AGN obscured by material on ISM rather than nuclear scales, as an alternative explanation.

The similarities between HRQs and the LRDs are evident, however, the physical properties of these AGN differ from HRQs. LRDs are significantly less luminous than their cosmic-noon cousins, hosting black-hole masses $\sim 10^6-10^8$ M$_\odot$yr^{-1} and $\lambda_{\rm Edd} \sim 1$ (Kocevski et al. 2024). Not only are they probing different regions of the quasar luminosity function, but also different regions of the M$_{\rm BH}$–$\lambda_{\rm Edd}$ plane. Despite this, it is clear that obscured accretion plays a major role in black-hole growth across the full dynamic range of black-hole mass and redshift.

5 CONCLUSIONS

We have presented a high-resolution rest-frame UV to optical X-Shooter spectrum of a hyperluminous HRQ at $z = 2.566$ – ULASJ2315+0143 . We spectroscopically confirm the presence of excess UV emission relative to a dust-reddened quasar SED, which was initially noted in broad-band photometric observations of this source. We fit the spectrum with several composite SED models to simultaneously explain the dust-attenuated rest-frame optical and excess rest-frame UV emission and also conduct a comprehensive analysis of the numerous emission and absorption line features detected in the spectrum. Our main findings are as follows:

(i) We confirm that the blue photometric colours of this source (Wethers et al. 2018) can not be explained by a simple dust-attenuated quasar model. If a secondary AGN component is responsible for the excess UV emission as seems likely based on the detection of broad emission lines in the UV, the luminosity of this blue AGN component is just 0.05 per cent of the total luminosity inferred from the dust-attenuated quasar component which has $\log_{10}\{\lambda {\rm L}_\lambda(3000\,\AA)[{\rm erg\ s^{-1}}]\} = 47.9$ and a dust extinction of $E(B-V)^{\rm QSO} = 1.55$ mag. Based on analysis of the rest-frame UV imaging for this source, we rule out the presence of a dual AGN system. We conclude that we would require an extremely contrived dust geometry for just 0.05 per cent of the intrinsic AGN emission to 'leak' through the obscuring medium and we therefore suggest that scattered AGN light scattering off dust in the ISM of the host galaxy can explain the broad emission lines seen in the rest-frame UV and potentially the UV continuum emission.

(ii) We detect narrow [O II] emission without any significant emission from either [Ne III] or [Ne V] and we therefore suggest that at least some of this [O II] emission is likely coming from the star-forming host galaxy of the dusty quasar. We also detect narrow Lyα emission at the systemic redshift of the quasar with an EW and Lyα to NV ratio that is much higher than typically observed in blue quasars. Once again, some contribution from a star-forming host galaxy could be responsible for the narrow Lyα emission. Finally a composite dusty quasar + star-forming host galaxy fit to the X-Shooter spectrum provides a good match to the rest-frame UV and optical continuum shape though of course it cannot reproduce the broad emission lines in the UV. We conclude that the narrow low-ionization nebular emission lines seen in the spectrum and potentially some of the UV continuum could also be coming from the quasar host galaxy. This is corroborated by analysis of the rest-frame UV image of this source from HyperSuprimeCam which shows evidence for spatially extended emission.

(iii) We analyse the mid-infrared SED of ULASJ2315+0143 in an attempt to constrain the location of any dust that is responsible for attenuating the quasar emission and also potentially scattering some of the rest-frame UV emission to our line of sight. We find that ULASJ2315+0143 has an extremely flat and atypical mid-infrared SED with a ratio between the hot dust and accretion disc component at 2 μm that is at least a factor of 5 lower than the average blue SDSS quasar at the same redshift. This suggests significant depletion of any hot (> 1000 K) dust component on toroidal scales. Hence, we propose that the bulk of the obscuring medium is on ISM, rather than nuclear, scales. An extended scattering medium is consistent with the blueshifts observed in the rest-frame UV high-ionization lines – for example, C IV and N V, since a dense circumnuclear cocoon would

Downloaded from https://academic.oup.com/mnras/article/533/3/2948/7733827 by guest on 07 November 2024

likely result in the symmetrical line profiles such as those observed in ERQs.

(iv) We detect numerous AAL systems in the rest-frame UV across a range of species and velocity components including blueshifted absorption features in C IV, N V, Si IV, and Si III as well as potentially redshifted features in Si III and C IV.

(v) Using the Balmer lines and the optical continuum luminosity (L_λ(5100 Å)), we estimate the black-hole mass $\log_{10}(\mathrm{H}\beta, \mathrm{MBH}[\mathrm{M}_\odot]) = 10.26 \pm 0.05$, bolometric luminosity $L_{\mathrm{Bol}} = 10^{48.16}$ erg s^{-1} and Eddington-scaled accretion rate $\log_{10}(\lambda_{\mathrm{Edd}}) = -0.19$. Our optical-derived bolometric luminosity implies an X-ray bolometric correction $\log_{10}(\mathrm{k_{Bol}}, \mathrm{L_X}) = 2.56$. The bolometric correction implied from the mid-infrared luminosity $\log_{10}(\mathrm{k_{Bol}}, \mathrm{L}_{6\mu\mathrm{m}}) = -0.66$.

(vi) We find evidence for significant outflows affecting both the BLR and NLR gas. The C IV blueshift is 1080±110 km s^{-1} and the [O III] W80 is 1830±350 km s^{-1}. However, in the context of outflows seen in other luminous quasar populations, these values are not extreme and could be explained by the significant black hole mass of ULASJ2315+0143 . Using the [O III] velocity, we estimate the mass outflow rate for the ionized gas $\dot{M}^{\mathrm{out}}_{\mathrm{ion}} = 199\,\mathrm{M}_\odot\,\mathrm{yr}^{-1}$, with a corresponding kinetic power $\dot{\epsilon}^{ion}_k = 10^{44.61}\mathrm{erg\,s}^{-1} \sim 0.001\,\mathrm{L_{Bol}}$. This is consistent with SDSS blue quasars at comparable luminosity.

(vii) Despite probing a different region of the quasar luminosity function and MBH–λ_{Edd} plane, we find that ULASJ2315+0143 represents a cosmic-noon analogue of the *JWST* LRDs. Both LRDs and HRQs exhibit blue rest-frame UV photometric colours, which are interpreted as some combination of scattered AGN and star-forming host galaxy emission. As both populations show signs of hot dust depletion in their mid-infrared SEDs, we propose that the obscuring medium in both populations is likely on galaxy-wide rather than torus scales.

Over the coming years, large spectroscopic surveys in the NIR, for example, with VLT-MOONS (Maiolino et al. 2020) and the Prime Focus Spectrograph (Greene et al. 2022) will offer the opportunity to characterize the properties of many more red AGN effectively bridging the gap in both luminosity and redshift between HRQs such as ULASJ2315+0143 and the *JWST* LRD population.

ACKNOWLEDGEMENTS

We thank Jenny Greene for a constructive referee's report and Christian Knigge and James Matthews for their invaluable insight, which helped shape the discussion. We also thank J. Xavier Prochaska and the PYPEIT user community for advice on using PYPEIT during the data-reduction stages of this work.

MS acknowledges funding from the University of Southampton via the Mayflower studentship. MB, ST, and SM acknowledge funding from the Royal Society via a University Research Fellowship Renewal Grant and Research Fellows Enhancement Award (URF/R/221103; RF/ERE/221053). MT acknowledges funding from the Science and Technology Funding Council (STFC) grant, ST/X001075/1.

DATA AVAILABILITY

The X-Shooter data presented in this paper can be downloaded from the European Southern Observatory's (ESO) online archive,[7] with ESO Program ID: 099.A-0755(A).

[7]http://archive.eso.org/eso/eso_archive_main.html

REFERENCES

Alexandroff R. M. et al., 2018, MNRAS, 479, 4936
Assef R. J. et al., 2015, ApJ, 804, 27
Assef R. J. et al., 2020, ApJ, 897, 112
Assef R. J. et al., 2022, ApJ, 934, 101
Banerji M., McMahon R. G., Hewett P. C., Alaghband-Zadeh S., Gonzalez-Solares E., Venemans B. P., Hawthorn M. J., 2012, MNRAS, 427, 2275
Banerji M., McMahon R. G., Hewett P. C., Gonzalez-Solares E., Koposov S. E., 2013, MNRAS, 429, L55
Banerji M., Alaghband-Zadeh S., Hewett P. C., McMahon R. G., 2015, MNRAS, 447, 3368
Banerji M., Carilli C. L., Jones G., Wagg J., McMahon R. G., Hewett P. C., Alaghband-Zadeh S., Feruglio C., 2017, MNRAS, 465, 4390
Banerji M., Jones G. C., Wagg J., Carilli C. L., Bisbas T. G., Hewett P. C., 2018, MNRAS, 479, 1154
Banerji M., Jones G. C., Carniani S., DeGraf C., Wagg J., 2021, MNRAS, 503, 5583
Begelman M. C., Blandford R. D., Rees M. J., 1980, Nature, 287, 307
Benson A. J., Bower R. G., Frenk C. S., Lacey C. G., Baugh C. M., Cole S., 2003, ApJ, 599, 38
Birrer S. et al., 2021, J. Open Source Softw., 6, 3283
Bischetti M. et al., 2017, A&A, 598, A122
Calistro Rivera G. et al., 2021, A&A, 649, A102
Calzetti D., Armus L., Bohlin R. C., Kinney A. L., Koornneef J., Storchi-Bergmann T., 2000, ApJ, 533, 682
Cano-Díaz M., Maiolino R., Marconi A., Netzer H., Shemmer O., Cresci G., 2012, A&A, 537, L8
Chen C., Hamann F., Simon L., Barlow T., 2018, MNRAS, 481, 3865
Coatman L., Hewett P. C., Banerji M., Richards G. T., Hennawi J. F., Prochaska J. X., 2019, MNRAS, 486, 5335
Cole S. et al., 2001, MNRAS, 326, 255
Conselice C. J., Bershady M. A., Dickinson M., Papovich C., 2003, AJ, 126, 1183
Costa T., Rosdahl J., Sijacki D., Haehnelt M. G., 2018, MNRAS, 479, 2079
Czerny B., Li J., Loska Z., Szczerba R., 2004, MNRAS, 348, L54
Di Matteo T., Springel V., Hernquist L., 2005, Nature, 433, 604
Ding X., Silverman J., Birrer S., Treu T., Tang S., Yang L., Bottrell C., 2022, Astrophysics Source Code Library, record ascl:2209.011
Dubois Y., Peirani S., Pichon C., Devriendt J., Gavazzi R., Welker C., Volonteri M., 2016, MNRAS, 463, 3948
Eisenhardt P. R. M. et al., 2012, ApJ, 755, 173
Fabian A. C., 2012, ARA&A, 50, 455
Fawcett V. A., Alexander D. M., Rosario D. J., Klindt L., Fotopoulou S., Lusso E., Morabito L. K., Calistro Rivera G., 2020, MNRAS, 494, 4802
Fawcett V. A., Alexander D. M., Rosario D. J., Klindt L., Lusso E., Morabito L. K., Calistro Rivera G., 2022, MNRAS, 513, 1254
Fawcett V. A. et al., 2023, MNRAS, 525, 5575
Foltz C. B., Weymann R. J., Peterson B. M., Sun L., Malkan M. A., Chaffee Frederic H. J., 1986, ApJ, 307, 504
Gallerani S. et al., 2010, A&A, 523, A85
Gillette J., Hamann F., Lau M. W., Perrotta S., 2024, MNRAS, 527, 950
Giustini M., Proga D., 2019, A&A, 630, A94
Glikman E. et al., 2012, ApJ, 757, 51
Glikman E., Simmons B., Mailly M., Schawinski K., Urry C. M., Lacy M., 2015, ApJ, 806, 218
Goodman J., Weare J., 2010, Commun. Appl. Math. Comput. Sci., 5, 65
Goulding A. D. et al., 2018, ApJ, 856, 4
Granato G. L., Zotti G. D., Silva L., Bressan A., Danese L., 2004, ApJ, 600, 580
Greene J. E., Ho L. C., 2005, ApJ, 630, 122
Greene J., Bezanson R., Ouchi M., Silverman J., the PFS Galaxy Evolution Working Group, 2022, preprint (arXiv:2206.14908)
Greene J. E. et al., 2024, ApJ, 964, 39
Guo H., Shen Y., Wang S., 2018, Astrophysics Source Code Library, record ascl:1809.008
Habouzit M. et al., 2021, MNRAS, 503, 1940

Downloaded from https://academic.oup.com/mnras/article/533/3/2948/7733827 by guest on 07 November 2024

Hamann F., Kanekar N., Prochaska J. X., Murphy M. T., Ellison S., Malec A. L., Milutinovic N., Ubachs W., 2011, MNRAS, 410, 1957
Hamann F. et al., 2017, MNRAS, 464, 3431
Hao C.-N., Kennicutt R. C., Johnson B. D., Calzetti D., Dale D. A., Moustakas J., 2011, ApJ, 741, 124
Harrison C. M., Ramos Almeida C., 2024, Galaxies, 12, 17
Hewett P. C., Wild V., 2010, 405, 2302
Hönig S. F., 2019, ApJ, 884, 171
Hopkins P. F., Elvis M., 2009, MNRAS, 401, 7
Hopkins P. F., Hernquist L., Cox T. J., Di Matteo T., Martini P., Robertson B., Springel V., 2005, ApJ, 630, 705
Hopkins P. F., Hernquist L., Cox T. J., Kereš D., 2008, ApJS, 175, 356
Horne K., 1986, Publ. Astron. Soc. Pac., 98, 609
Huang J. S., Glazebrook K., Cowie L. L., Tinney C., 2003, ApJ, 584, 203
Ishibashi W., Banerji M., Fabian A. C., 2017, MNRAS, 469, 1496
Kawanomoto S. et al., 2018, Publ. Astron. Soc. Japan, 70, 66
Kennicutt Robert C. J., 1998, ARA&A, 36, 189
Kennicutt R. C., Evans N. J., 2012, ARA&A, 50, 531
Klindt L., Alexander D. M., Rosario D. J., Lusso E., Fotopoulou S., 2019, MNRAS, 488, 3109
Kocevski D. D. et al., 2023, ApJ, 954, L4
Kocevski D. D. et al., 2024, preprint (arXiv:2404.03576)
Kormendy J., Ho L. C., 2013, ARA&A, 51, 511
Koss M. J. et al., 2023, ApJ, 942, L24
Lansbury G. B., Banerji M., Fabian A. C., Temple M. J., 2020, MNRAS, 495, 2652
López-Sanjuan C. et al., 2012, A&A, 548, A7
Maddox N., 2018, MNRAS, 480, 5203
Magorrian J. et al., 1998, AJ, 115, 2285
Maiolino R. et al., 2020, The Messenger, 180, 24
Martocchia S. et al., 2017, A&A, 608, A51
Matthee J. et al., 2024, ApJ, 963, 129
Murphy E. J. et al., 2011, ApJ, 737, 67
Nestor D., Hamann F., Rodriguez Hidalgo P., 2008, MNRAS, 386, 2055
Netzer H., 2019, MNRAS, 488, 5185
Noboriguchi A. et al., 2019, ApJ, 876, 132
Onoue M. et al., 2023, ApJ, 942, L17
Pensabene A., Carniani S., Perna M., Cresci G., Decarli R., Maiolino R., Marconi A., 2020, A&A, 637, A84
Pérez-González P. G. et al., 2024, ApJ, 968, 4
Perrotta S., Hamann F., Zakamska N. L., Alexandroff R. M., Rupke D., Wylezalek D., 2019, MNRAS, 488, 4126
Pillepich A. et al., 2017, MNRAS, 473, 4077
Prochaska J. X. et al., 2020a, pypeit/PypeIt: Release 1.0.0
Prochaska J. X. et al., 2020b, J. Open Source Softw., 5, 2308
Puglisi A. et al., 2017, ApJ, 838, L18
Rankine A. L., Hewett P. C., Banerji M., Richards G. T., 2020, MNRAS, 492, 4553
Richards G. T. et al., 2003, AJ, 126, 1131
Richards G. T. et al., 2011, AJ, 141, 167
Rosas-Guevara Y. M., Bower R. G., McAlpine S., Bonoli S., Tissera P. B., 2019, MNRAS, 483, 2712
Sawicki M., 2002, AJ, 124, 3050
Schaye J. et al., 2015, MNRAS, 446, 521
Shen Y., 2016, ApJ, 817, 55
Shen Y., Ménard B., 2012, ApJ, 748, 131
Shen Y. et al., 2011, ApJS, 194, 45
Silverman J. D. et al., 2020, ApJ, 899, 154
Simpson J. M. et al., 2014, ApJ, 788, 125
Somerville R. S., Hopkins P. F., Cox T. J., Robertson B. E., Hernquist L., 2008, MNRAS, 391, 481
Steinborn L. K., Dolag K., Comerford J. M., Hirschmann M., Remus R.-S., Teklu A. F., 2016, MNRAS, 458, 1013
Stepney M., Banerji M., Hewett P. C., Temple M. J., Rankine A. L., Matthews J. H., Richards G. T., 2023, MNRAS, 524, 5497
Tang S. et al., 2021, ApJ, 922, 83
Temple M. J., Banerji M., Hewett P. C., Coatman L., Maddox N., Peroux C., 2019, MNRAS, 487, 2594
Temple M. J., Banerji M., Hewett P. C., Rankine A. L., Richards G. T., 2021a, MNRAS, 501, 3061
Temple M. J., Hewett P. C., Banerji M., 2021b, MNRAS, 508, 737
Temple M. J. et al., 2023, MNRAS, 523, 646
Temple M. J. et al., 2024, MNRAS, 532, 424
Tripp T. M., Lu L., Savage B. D., 1998, ApJ, 508, 200
Urrutia T., Lacy M., Becker R. H., 2008, ApJ, 674, 80
Urrutia T., Becker R. H., White R. L., Glikman E., Lacy M., Hodge J., Gregg M. D., 2009, ApJ, 698, 1095
Vanden Berk D. et al., 2008, ApJ, 679, 239
Veilleux S. et al., 2009, ApJS, 182, 628
Veilleux S. et al., 2023, ApJ, 953, 56
Vernet J. et al., 2011, A&A, 536, A105
Vestergaard M., Peterson B. M., 2006, ApJ, 641, 689
Villar Martín M., Perna M., Humphrey A., Castro Rodríguez N., Binette L., Pérez González P. G., Mateos S., Cabrera Lavers A., 2020, A&A, 634, A116
Volonteri M., Dubois Y., Pichon C., Devriendt J., 2016, MNRAS, 460, 2979
Weedman D., Sargsyan L., Lebouteiller V., Houck J., Barry D., 2012, ApJ, 761, 184
Wethers C. F. et al., 2018, MNRAS, 475, 3682
Wild V. et al., 2008, MNRAS, 388, 227
Williams C. C. et al., 2024, ApJ, 968, 34
Wylezalek D. et al., 2022, ApJ, 940, L7
Yue M., Fan X., Yang J., Wang F., 2021, ApJ, 921, L27
Zakamska N. L. et al., 2016, MNRAS, 459, 3144

APPENDIX A: PYPEIT REDUCTION PARAMETERS

For reproduciblity, we detail the PYPEIT user-level parameters that were changed from their default values to reduce the raw spectrum of ULASJ2315+0143 in Table A1.

Downloaded from https://academic.oup.com/mnras/article/533/3/2948/7733827 by guest on 07 November 2024

Table A1. We present the various PYPEIT user-level parameters used to optimize the reduction and extraction of the ULASJ2315+0143 X-Shooter spectrum.

UVB/VIS		
Primary block	Secondary block	Parameter
Reduce	findobj	snr_thresh = 3.0
Reduce	findobj	ech_find_max_snr = 1.0
Reduce	findobj	ech_find_min_snr = 0.1
Reduce	findobj	ech_find_nabove_min_snr = 2.0
Calibrations	wavelengths	rms_threshold = 2.0
Calibrations	tilts	sig_neigh = 5.0
Calibrations	tilts	tracethresh = 5.0
Calibrations	slitedges	tracethresh = 7.0
NIR		
Primary block	Secondary block	Parameter
Reduce	N/A	trim_edge = 1,1
Reduce	findobj	find_trim_edge = 1,1
Reduce	findobj	snr_thresh = 5.0
Reduce	findobj	ech_find_max_snr = 1.0
Reduce	findobj	ech_find_min_snr = 0.1
Reduce	findobj	ech_find_nabove_min_snr = 2.0
Reduce	skysub	no_local_sky = True
Reduce	skysub	global_sky_std = False
Reduce	extraction	use_2dmodel_mask = False
Calibrations	wavelengths	rms_threshold = 1.1
Calibrations	tilts	sig_neigh = 5.0
Calibrations	tilts	tracethresh = 5.0
Calibrations	slitedges	tracethresh = 7.0

Note. The numerous additional parameters, which do not feature in this table, were left at their default settings.

APPENDIX B: DEGENERACIES IN THE REDDENED QUASAR + BLUE QUASAR LIGHT SED MODEL

Here, we discuss the degeneracies in the model parameters associated with the first SED fit detailed in Section 3.2. We present the corner plot for this SED model in Fig. B1. The marginalized distributions show that each parameter is well converged, however, Fig. B1 reveals several degeneracies. We observe a strong anticorrelation between $f_{\rm UV}$ and both $\log_{10}\{\lambda L_\lambda(3000\AA)\}$ and $E(B-V)^{\rm QSO}$, which, in turn, are positively correlated with each other. This behaviour is expected as should the quasar be more luminous, a lower scattering fraction is required to reproduce the rest-frame UV emission. Equally, should the quasar suffer heavier dust attenuation, we require a more luminous quasar to reproduce the rest-frame optical and hence the scattering fraction must again be lower to compensate for the increase in luminosity. The emline_type parameter is independent of the other three model parameters since the Temple et al. (2021b) SED model allows for line strength variations independent of the continuum parameters.

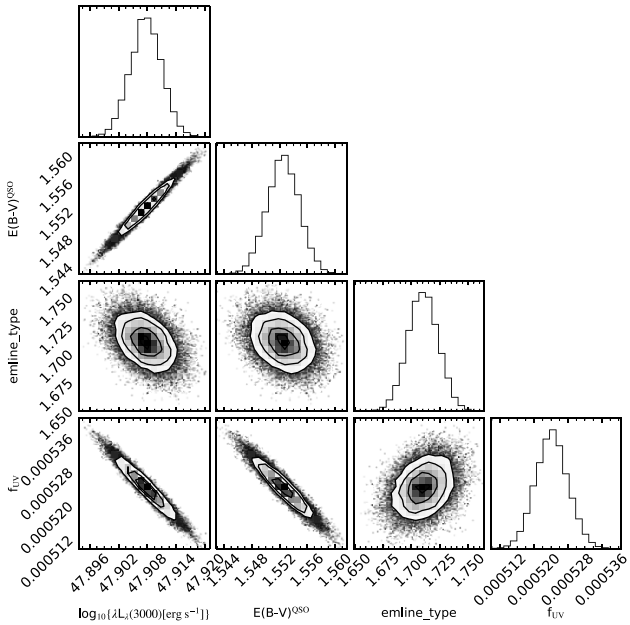

Figure B1. The reddened quasar + blue quasar light SED model (see Section 3.2) corner plots. In order left-to-right/top-to-bottom panels, the marginalized distributions represent $\log_{10}\{\lambda L_\lambda(3000\AA)\}$, $E(B-V)^{\rm QSO}$, emline_type and $f_{\rm UV}$. The corner plot illustrates that the model is well-converged and highlights the degeneracies between several model parameters.

This paper has been typeset from a TEX/LATEX file prepared by the author.

Downloaded from https://academic.oup.com/mnras/article/533/3/2948/7733827 by guest on 07 November 2024

© 2024 The Author(s).
Published by Oxford University Press on behalf of Royal Astronomical Society. This is an Open Access article distributed under the terms of the Creative Commons Attribution License (https://creativecommons.org/licenses/by/4.0/), which permits unrestricted reuse, distribution, and reproduction in any medium, provided the original work is properly cited.